RESEARCH ARTICLE

Development of nanoscale structure in LAT-based signaling complexes

Valarie A. Barr[1], Eilon Sherman[2], Jason Yi[1], Itoro Akpan[1], Alexandre K. Rouquette-Jazdanian[1] and Lawrence E. Samelson[1],*

ABSTRACT

The adapter molecule linker for activation of T cells (LAT) plays a crucial role in forming signaling complexes induced by stimulation of the T cell receptor (TCR). These multi-molecular complexes are dynamic structures that activate highly regulated signaling pathways. Previously, we have demonstrated nanoscale structure in LAT-based complexes where the adapter SLP-76 (also known as LCP2) localizes to the periphery of LAT clusters. In this study, we show that initially LAT and SLP-76 are randomly dispersed throughout the clusters that form upon TCR engagement. The segregation of LAT and SLP-76 develops near the end of the spreading process. The local concentration of LAT also increases at the same time. Both changes require TCR activation and an intact actin cytoskeleton. These results demonstrate that the nanoscale organization of LAT-based signaling complexes is dynamic and indicates that different kinds of LAT-based complexes appear at different times during T cell activation.

KEY WORDS: Photoactivated localization microscopy, T cell activation, Signaling complex, Microcluster, Single-molecule localization microscopy, Nanostructure

INTRODUCTION

Activation of the T cell antigen receptor (TCR) is a key event in the initiation of adaptive immune responses. The TCR engages a peptide antigen bound to a cell surface protein encoded by the major histocompatibility complex genes (MHC) on an antigen-presenting cell (APC), triggering the recruitment of scaffold and effector proteins into complexes that initiate signal transduction (Rajasekaran et al., 2016). Many of the participants in TCR-based signaling have been identified, including linker for activation of T cells (LAT), a crucial adapter protein that is recruited to signaling complexes and then phosphorylated on several tyrosine residues. Phosphorylated LAT serves as a binding platform for other SH2-domain-containing components, such as Grb2, Gads (also known as GRAP2) and PLC-γ1 (Balagopalan et al., 2010; Zhang et al., 1999a). Another crucial adapter protein, SLP-76 (also known as LCP2), is bound constitutively to Gads and is brought into LAT-based complexes when Gads binds to LAT. SLP-76 is also phosphorylated on multiple tyrosine residues, producing additional docking sites for important effector molecules such as Nck (also known as Nck1), Vav (also known as Vav1) and Itk (Clements, 2003; Myung et al., 2001). Cooperative interactions are important in LAT-based complexes. PLC-γ1 binds to both LAT and SLP-76 and interaction with both proteins is needed to stabilize the association of PLC-γ1 with signaling complexes (Barda-Saad et al., 2010; Braiman et al., 2006). These two essential adapter proteins are both needed for proper signal transduction, T cell activation and subsequent immune responses (Yablonski et al., 1998; Zhang et al., 1999b). Recent work has shown that signal transduction from TCR phosphorylation through LAT and SLP-76 clustering to activation of actin polymerization can be reconstructed in vitro (Su et al., 2016).

LAT-based oligomers appear to be important for activation of several downstream signaling pathways (Kortum et al., 2013). Grb2 can bind to any one of three tyrosine residues on LAT while simultaneously binding Sos1, and Sos1 can bind two Grb2 molecules, potentially forming a meshwork of cross-linked LAT molecules (Houtman et al., 2006; Kortum et al., 2013). Depletion of Grb2, loss of Sos1 or mutation of LAT to prevent multipoint Grb2 binding all cause decreased ERK activation, PLC-γ1 phosphorylation and diminished Ca^{2+} flux (Balagopalan et al., 2015). SLP-76 oligomers are also important for T cell activation. SLP-76 can be crosslinked by multipoint binding to the adapter protein ADAP (also known as FYB) at three phosphorylation sites (Boerth et al., 2000; da Silva et al., 1997). Removing two of these sites prevents crosslinking and leads to decreased Ca^{2+} flux. Thus, it appears that some level of oligomerization of LAT and SLP-76 is required to produce proper T cell activation (Coussens et al., 2013).

Imaging studies have shown that TCR engagement leads to dramatic changes in T cells, including the rapid formation of discrete puncta termed microclusters (Balagopalan et al., 2011; Yokosuka and Saito, 2010). These microclusters have been studied extensively in T cells activated by peptide–MHC (pMHC) on an APC (Freiberg et al., 2002; Johnson et al., 2000; Krummel et al., 2000; Lee et al., 2002), through use of activating molecules incorporated into lipid bilayers (Campi et al., 2005; Grakoui et al., 1999; Ilani et al., 2009; Kaizuka et al., 2007; Yokosuka et al., 2005) and activating antibodies on glass surfaces (Barda-Saad et al., 2005; Bunnell et al., 2002, 2001). Microclusters initially contain most of the molecules required for TCR signaling, including both LAT and SLP-76 and they appear to be the sites where signal transduction begins (Bunnell et al., 2002; Varma et al., 2006; Yokosuka et al., 2005). Live-cell studies have shown that microclusters are dynamic structures, as constituents of the signaling complexes continuously dissociate and re-associate (Bunnell et al., 2002). Furthermore, the composition of signaling complexes changes as the cells spread; some proteins such as Gads and Cbl are only seen transiently in microclusters and are not present in microclusters visualized at later times (Balagopalan et al., 2007; Bunnell et al., 2002).

[1]Laboratory of Cellular and Molecular Biology, CCR, NCI, NIH, Bethesda, MD 20892, USA. [2]Racah Institute of Physics, The Hebrew University, Jerusalem 91904, Israel.

*Author for correspondence (samelsonl@helix.nih.gov)

V.A.B., 0000-0001-5377-4753; E.S., 0000-0002-7403-6036; J.Y., 0000-0001-5131-6767; I.A., 0000-0002-3239-6252; A.K.R., 0000-0003-2646-0040; L.E.S., 0000-0002-5963-2112

To understand the dynamic organization and potential heterogeneity of the signaling complexes induced by TCR engagement, we need to determine their molecular structures at various times after activation. Many researchers have turned to super-resolution microscopy techniques to observe molecular details beyond the diffraction limit of visible light (Nienhaus and Nienhaus, 2016; Sydor et al., 2015). Single-molecule localization microscopy (SMLM) has been used to visualize molecules found in microclusters at high resolution (Hsu and Baumgart, 2011; Lillemeier et al., 2010; Purbhoo et al., 2010; Rossy et al., 2013; Sherman et al., 2011). In SMLM, the center of a diffraction-limited spot produced by a single fluorescently labeled molecule is determined mathematically and defined as the probable location of the molecule (Allen et al., 2013; Knight, 2017). A small cohort of activated molecules is imaged and then they are photoswitched or photobleached. Another cohort of molecules can then be activated and the entire process is repeated many times to visualize thousands of single molecules. The position of each individual molecule is calculated from the corresponding diffraction-limited spot in the image series. These calculated positions, often called molecular peaks or localizations, are combined to produce an image showing the location of every visualized molecule. Two common methods are photo-activation localization microscopy (PALM) (Betzig et al., 2006; Sengupta et al., 2014) and direct stochastic optical resolution microscopy (dSTORM) (Endesfelder and Heilemann, 2015; Heilemann et al., 2008; van de Linde et al., 2011).

PALM and dSTORM have been used to examine T cell signaling complexes in several studies. The organization of many molecules has been studied including the TCR, Lck, ZAP-70, Grb2, LAT and SLP-76 (Hsu and Baumgart, 2011; Lillemeier et al., 2010; Neve-Oz et al., 2015; Purbhoo et al., 2010; Rossy et al., 2013; Sherman et al., 2011). Several of these studies have shown that, even in the absence of TCR stimulation, LAT is organized into small clusters or nanoclusters. Our previous PALM study indicated that most clusters contain only two or three molecules of LAT conjugated to a photoactivatable protein (Sherman et al., 2011). The extent of LAT clustering increases modestly after TCR engagement. Similar results were found using high-speed PALM (Lillemeier et al., 2010). Studies on LAT mutants have shown that the phosphorylated tyrosine residues that are responsible for protein–protein interactions and the lipid-modified cysteine residues that are required for association with ordered membrane domains are both involved in LAT nanoclustering (Sherman et al., 2011). The nanoscale LAT organization also requires an intact actin network (Sherman et al., 2011). These data suggest that LAT nanostructure requires contributions from membrane domains, protein–protein interactions and cytoskeletal elements.

Two-color SMLM has shown a variety of interactions between LAT and other proteins. The TCR and LAT form small clusters that tend to be segregated from each other (Lillemeier et al., 2010; Sherman et al., 2011), with some overlap at 'hotspots' (Sherman et al., 2011). ZAP-70 kinase mixes uniformly with TCR but shows only partial mixing with LAT. Grb2 mixes well with LAT throughout the cell. Given that most LAT is in small nanoclusters, this suggests that all LAT clusters, even the smallest ones, contain phosphorylated LAT and are capable of binding at least one downstream effector. Sherman et al. also demonstrated that LAT and SLP-76 do not mix well and are organized within the signaling clusters themselves, with LAT tending to be in the center and SLP-76 distributed on the outside (Sherman et al., 2011).

Because microclusters are dynamic structures, we were interested in how the nanostructure of LAT-based complexes changes with time. In this study, we present a detailed examination of LAT and SLP-76 nanostructure in the first few minutes following TCR activation and the initiation of cell spreading.

RESULTS

In our previous experiments, PALM images were obtained of Jurkat T cells several minutes after plating onto stimulatory coverslips. These well-spread cells were flattened against the stimulatory surface and generally had large, circular footprints. Examination of the PALM images showed a non-random distribution of LAT and SLP-76, where SLP-76 molecules tended to localize to the edges of LAT clusters (Sherman et al., 2011). In the current study, we asked how this nanostructure develops during T cell activation.

First, we captured movies of live Jurkat T cells expressing LAT–YFP contacting an anti-CD3-coated coverslip using total internal reflection fluorescence (TIRF) microscopy (Movie 1). TIRF illumination confines the excitation energy to a narrow zone near the coverslip so we can easily observe the formation of LAT clusters (Toomre and Manstein, 2001). Although SLP-76 and LAT are internalized into mobile structures following activation, these endocytic structures are not well visualized by TIRF microscopy (Barr et al., 2006). Thus, the clusters studied here are predominantly surface clusters. We then identified three phases in the spreading process (Fig. S1). When a T cell contacted a stimulatory surface, microclusters developed on the cell extensions that first touched the surface (Fig. S1A). The cells then spread on the activating surface (Fig. S1B), eventually forming a relatively round, well-spread cell (Fig. S1C). We termed cells that were developing the first contacts 'Class 1 cells'. Cells that had begun to spread but had not yet reached their full extension were called 'Class 2 cells' and fully spread cells were called 'Class 3 cells'. For analysis, fixed cells were grouped into these classes after examining the raw images of conjugated LAT in the unprocessed PALM images and a corresponding brightfield image (see Fig. S1E and Materials and Methods for details). Class 1 cells were generally found in fixed samples incubated for 2.5 min at 37°C, whereas Class 3 cells usually required 3 min of incubation. Class 2 cells could be found at both time points.

Having established a classification scheme, we obtained PALM images of Jurkat T cells expressing LAT–Dronpa and SLP-76 conjugated to photoactivatable mCherry (SLP–PA-mCherry) plated on anti-CD3-coated coverslips at different stages of the spreading process. Localization peaks representing the probable locations of the fluorophores were determined for both proteins. To account for multiple peaks emanating from a single fluorophore, localization peaks were combined based on a temporal gap and distance threshold. Combined or grouped peaks were then assigned to a single molecular location (see Materials and Methods). Bivariate pair-correlation functions (PCFs) generated by a published algorithm (Wiegand and A. Moloney, 2004) were used to determine whether the green dots representing LAT–Dronpa molecules mixed randomly with the red dots representing SLP–PA-mCherry molecules (Sherman et al., 2013). The sample bivariate PCF was compared to a random labeling model (RLM) that served as the null hypothesis. In this model, molecules of either type were placed randomly in the locations where molecules were found in the original sample, using the same number of each type of molecule as found in the sample. The highest and lowest of 19 RLM bivariate PCF curves were plotted on the sample graph with the sample bivariate PCF. The area between these two curves defined the location of the 95% confidence level; that is, 95% of all RLM distributions are expected to produce bivariate PCFs that lie between theses curves. A sample bivariate PCF within this area shows a distribution that corresponds to the RLM and that the two types of

molecules are thus randomly mixed. A sample bivariate PCF plotted below this area shows less mixing than would be expected from the RLM. A uniform bivariate PCF consisting of a horizontal line equal to one would indicate no interaction between the two types of molecules. Because each individual sample produces a unique bivariate PCF that is meaningful only with respect to the bivariate PCFs generated by the RLM for that sample, it is difficult to measure how the same two labels interacted in different cells. Previously, we developed the concept of 'overall extent of mixing' to quantify mixing in a cohort of cells (Sherman et al., 2011, 2013). This measure was obtained by comparing the height of the sample PCF to the y-value of the center of the 95% confidence level produced by 19 runs of the RLM at scales below 60 nm (essentially the y-intercepts). Thus, if the sample PCF was in the middle of the RLM 95% confidence level as it approached the y-intercept, the extent of mixing was 100%, indicating that the two labels are well-mixed in the sample. If the sample PCF was below the 95% confidence level as it approached the y-intercept, the extent of mixing was less than 100% and the two labels mixed less than expected according to the RLM. Mixing levels from individual samples can be averaged to determine the overall behavior of various pairs of molecules under different conditions. This measurement is generally insensitive to the failure to detect all proteins and uncertainty in localization accuracy (Sherman et al., 2016, 2013).

In PALM images of Class 1 cells that had just contacted the stimulatory surface, LAT–Dronpa and SLP–PA-mCherry colocalized in clusters and did not show any obvious segregation (Fig. 1A). The PALM data from a typical Class 1 cell was made into an image where grouped localizations were displayed as colored dots (Fig. 1Ai–iii), and the size and brightness of each dot represents the localization probability density or the likelihood that a molecule can be found in the spot. A small bright spot means that there is a high probability that a molecule is in that spot. A larger dimmer spot indicates that there is more uncertainty about the location of the molecule. Fig. 1Aii shows the bivariate analysis of a central region of interest (ROI) from that cell. The bivariate PCF of the sample data was near the gray area of the 95% confidence level of the RLM. Thus, LAT–Dronpa and SLP–PA-mCherry showed a pattern similar to the RLM in this sample. Fig. 1Aiii shows enlarged renderings of two representative clusters where the uniform mixing of LAT and SLP-76 molecules was apparent. Similar results were obtained for Class 2 cells (Fig. 1B). A rendering of PALM data from a representative cell (Fig. 1Bi), the bivariate analysis of a central ROI (Fig. 1Bii) and an enlarged view of representative clusters (Fig. 1Biii) all showed little difference from the RLM. Only Class 3 or well-spread cells showed a more organized distribution of SLP–PA-mCherry and LAT–Dronpa (Fig. 1C). Some separation of the molecules was seen in the rendering of the whole cell (Fig. 1Ci). The bivariate PCF of a central ROI from the sample cell fell below the gray area that marks the RLM, indicating that LAT and SLP-76 mixed less than was expected in a random distribution (Fig. 1Cii). Finally, SLP-76 molecules were observed on the outside of LAT clusters in the enlarged renderings of clusters (Fig. 1Ciii). We then calculated the extent of mixing for each class (Fig. 1D). In Class 1 cells, the average extent of mixing was 85±6.7% (mean±s.e.m.), where in Class 2, the average extent of mixing was 85±3.7%, indicating that in both cases, the two molecules are well mixed. In contrast, the extent of mixing in Class 3 was reduced to 60±4.1%, demonstrating that in fully spread cells, the two molecules were more segregated (P<0.001, one-factor ANOVA). Thus, the pattern that we previously reported in Class 3 cells takes time to develop.
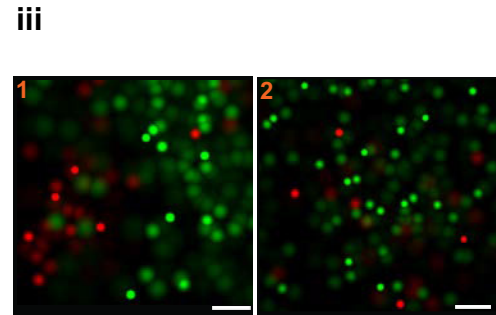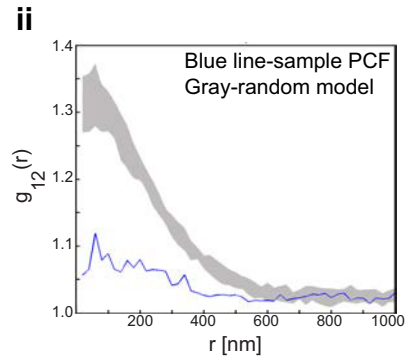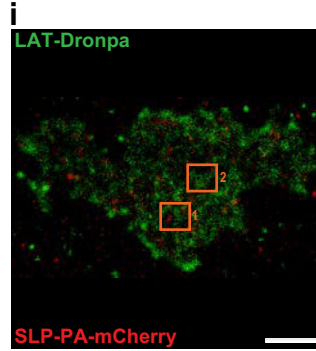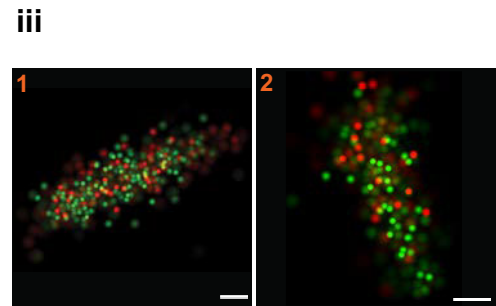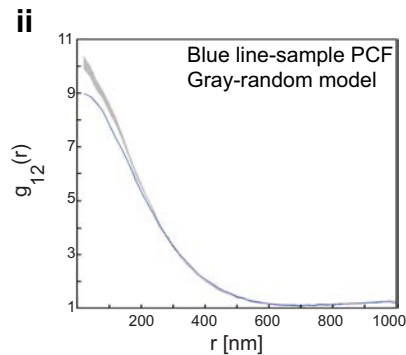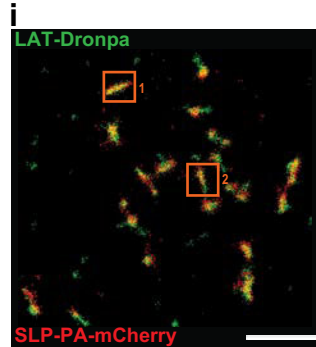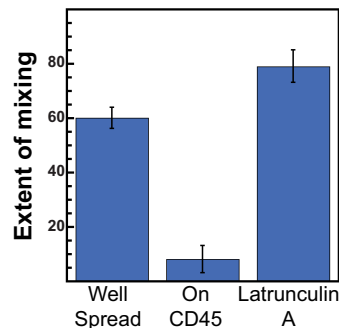
Development of LAT–SLP-76 nanostructure required TCR activation. There was no interaction between LAT–Dronpa and SLP–PA-mCherry in cells plated on non-activating anti-CD45-coated coverslips (Fig. 2A), because SLP-76 did not bind to LAT and remained in the cytosol. Therefore, very few SLP–PA-mCherry molecules were visualized in the PALM image as only a small amount of cytosol was within the TIRF excitation illumination (Fig. 2Ai,Aiii). The bivariate analysis curve of a central ROI was near one, the value expected when two molecules showed no interaction (Fig. 2Aii). The overall extent of mixing was 8±4.7% confirming little to no interaction between LAT and SLP in the absence of stimulation (Fig. 2C).

The development of LAT–SLP-76 nanostructure also required an intact actin cytoskeleton as LAT–Dronpa and SLP–PA-mCherry were well mixed in cells treated with Latrunculin A (Fig. 2B). After plating on a stimulatory coverslip, Latrunculin-A-treated cells were incubated for 4.5 min at 37°C to allow maximum spreading. The rendered cell showed a substantial interaction with the activating coverslip along with clustering of LAT–Dronpa and SLP–PA-mCherry at the contact sites (Fig. 2Bi). Bivariate analysis of the contact surface showed little difference from the RLM (Fig. 2Bii). The rendered clusters also showed uniform distributions of LAT and SLP (Fig. 2Biii). The extent of mixing was 79±6.4%, which was not significantly different from the extent of mixing in Class 1 and Class 2 cells (P=0.904, one-factor ANOVA), demonstrating that no separation occurred in the absence of an actin cytoskeleton (Fig. 2C).

Reports of molecular aggregation induced by PA-mCherry led us to perform additional control experiments (Wang et al., 2014a). The aggregation of conjugates of various fluorescent proteins with the bacterial Clp protein was used to study the self-association of proteins used for PALM imaging (Landgraf et al., 2012). Clp protein moieties interact weakly, so if the fluorescent protein tag also has a tendency to self-associate, aggregates of the fusion protein will be produced. PA-mCherry showed significant aggregation in this assay, whereas Dronpa showed little tendency to form aggregates (Wang et al., 2014a). To assess whether our results were influenced by the use of PA-mCherry, we examined Jurkat T cells expressing a chimeric construct expressing one of several T cell signaling proteins coupled to Dronpa as well as a construct where the same protein was conjugated to PA-mCherry. The transfected cells were plated onto stimulatory coverslips, fixed after 3 min of activation and examined by PALM. The two proteins would be expected to mix uniformly if there were no aggregation. The well-spread Class 3 cells expressing a mixture of TCRζ (also known as CD247) coupled to either Dronpa or PA-mCherry (TCRζ–Dronpa and TCRζ–PA-mCherry) were well-mixed as expected (Fig. 3A). A representative PALM rendering showed mixing throughout the cell (Fig. 3Ai), and bivariate analysis of a central ROI confirmed the mixing of the TCR molecules conjugated to the two fluorophores was similar to the RLM (Fig. 3Aii). Uniform mixing was also seen in individual clusters (Fig. 3Aiii). The overall extent of mixing was 87±1%. Similar results were obtained for mixing of SLP–Dronpa with SLP–PA-mCherry (Fig. 3B). Again, mixing of the two forms of SLP-76 was seen throughout the activated cell (Fig. 3Bi), as confirmed by bivariate analysis of a central ROI (Fig. 3Bii), mixing within individual clusters (Fig. 3Biii) and a high overall extent of mixing of 89±6.4%. In contrast, in cells containing both LAT–Dronpa and LAT–PA-mCherry, the two forms of labeled LAT molecules showed substantial segregation (Fig. 3C). This was visible in a rendering of a representative cell (Fig. 3Ci) and bivariate analysis of the two
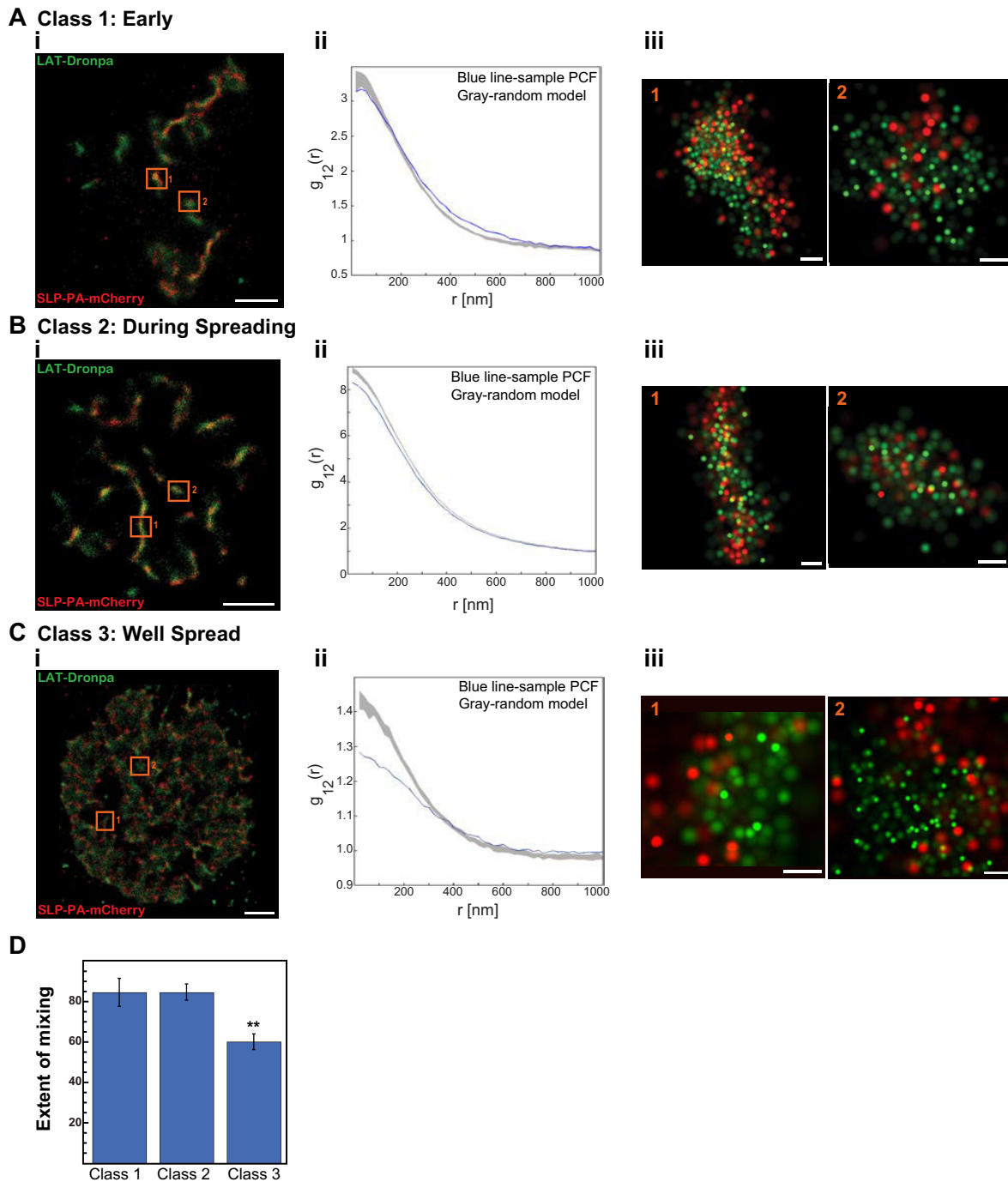
Fig. 1. LAT–SLP-76 nanostructure was seen only in well-spread Jurkat T cells. PALM images were obtained of Jurkat T cells expressing LAT–Dronpa and SLP–PA-mCherry at various times after contacting the coverslip. (A) LAT–Dronpa and SLP–PA-mCherry were well mixed in Class 1 cells fixed soon after contact with a stimulatory coverslip. (i) Rendering of a representative cell showing the localizations of LAT–Dronpa (green) and SLP–PA-mCherry (red). Color codes (brightest color is highest) for overlapping probability density functions of individual molecules, with maximal values of 3640 molecules/μm^2 for LAT–Dronpa and 1620 molecules/μm^2 for SLP–PA-mCherry. Scale bar: 2 μm. (ii) Bivariate analysis of a central ROI of the same cell. (iii) Renderings of clusters from the same cell, enlarged to show the relationship between LAT–Dronpa molecules and SLP–PA-mCherry molecules. (iii-1) Maximal values of 5230 molecules/μm^2 (green) and 3160 molecules/μm^2 (red). (iii-2) Maximal values of 6920 molecules/μm^2 (green) and 2490 molecules/μm^2 (red). Scale bars: 100 nm. (B) LAT–Dronpa and SLP–PA-mCherry were well mixed in Class 2 cells fixed partway through spreading. (i) Rendering of a representative cell showing the localizations of LAT–Dronpa (green) and SLP–PA-mCherry (red). Maximal values of 1860 molecules/μm^2 (green) and 1420 molecules/μm^2 (red). Scale bar: 2 μm. (ii) Bivariate analysis of a central ROI of the same cell. (iii) Renderings of enlarged clusters from the same cell. (iii-1) Maximal values of 3310 molecules/μm^2 (green) and 2160 molecules/μm^2 (red). (iii-2) Maximal values of 2180 molecules/μm^2 (green) and 1650 molecules/μm^2 (red). Scale bars: 100 nm. (C) LAT–Dronpa and SLP–PA-mCherry were more segregated in the well-spread Class 3 cells. (i) Rendering of a representative cell showing the localizations of LAT–Dronpa (green) and SLP–PA-mCherry (red). Maximal values of 2310 molecules/μm^2 (green) and 1220 molecules/μm^2 (red). Scale bar: 2 μm. (ii) Bivariate analysis of a central ROI of the same cell. (iii) Renderings of enlarged clusters from the same cell. (iii-1) Maximal values of 1680 molecules/μm^2 (green) and 1070 molecules/μm^2 (red). (iii-2) Maximal values of 3350 molecules/μm^2 (green) and 820 molecules/μm^2 (red). Scale bars: 100 nm. (D) Overall extent of mixing. Bars show s.e.m. Class 1, n=24 (five experiments); Class 2, n=21 (six experiments); Class 3, n=40 (six experiments). **P<0.004 between Class 1 and Class 3, two-tailed Student's t-test with unequal variance; no difference between Class 1 and Class 2.

Fig. 2. TCR stimulation and an intact actin cytoskeleton were needed for development of LAT–SLP-76 nanostructure. PALM images were obtained of Jurkat T cells expressing LAT–Dronpa and SLP–PA-mCherry. (A) No interaction was seen between LAT–Dronpa and SLP–PA-mCherry in cells plated on a non-stimulatory coverslip coated with anti-CD45 antibodies. (i) Rendering of a representative cell showing the localizations of LAT–Dronpa (green) and SLP–PA-mCherry (red). Maximal values of 1800 molecules/µm² (green) and 1700 molecules/µm² (red). Scale bar: 2 µm. (ii) Bivariate analysis of a central ROI of the same cell. (iii) Renderings of enlarged clusters from the same cell. (iii-1) Maximal values of 1840 molecules/µm² (green) and 2610 molecules/µm² (red). (iii-1) Maximal values of 3000 molecules/µm² (green) and 2340 molecules/µm² (red). Scale bars: 100 nm. (B) LAT–Dronpa and SLP–PA-mCherry were well mixed in cells treated with Latrunculin A. (i) Rendering of a representative cell showing the localizations of LAT–Dronpa (green) and SLP–PA-mCherry (red). Maximal values of 2850 molecules/µm² (green) and 1400 molecules/µm² (red). Scale bar: 2 µm. (ii) Bivariate analysis of a central ROI of the same cell. (iii) Renderings of clusters from the same cell, enlarged to show the relationship between LAT–Dronpa molecules and SLP–PA-mCherry molecules. (iii-1) Maximal values of 4900 molecules/µm² (green) and 3270 molecules/µm² (red). (iii-2) Maximal values of 5040 molecules/µm² (green) and 3570 molecules/µm² (red). Scale bars: 100 nm. (C) Overall extent of mixing. Bars show s.e.m. Class 3, n=40 (six experiments); plated on CD45, n=14 (three experiments); Latrunculin A treated, n=16 (two experiments).

forms of LAT in a central ROI gave a PCF well below that of the RLM (Fig. 3Cii). In enlarged images, clumps of LAT–PA-mCherry often appeared to be distinct from LAT–Dronpa (Fig. 3Ciii). The overall extent of mixing was 63±5.7% confirming the segregation of LAT–Dronpa from LAT–PA-mCherry in multiple cells.

Interestingly, the segregation of LAT–Dronpa molecules from LAT–PA-mCherry molecules also required TCR activation. Segregation leading to a lowered extent of mixing developed during spreading and was only seen in well-spread cells (Fig. 4A–C). In Class 1 cells, the extent of mixing was 92±2.8%, whereas in Class 2 cells, the extent of mixing was 88±5.5%. Segregation did not occur

in cells plated on anti-CD45-coated coverslips, where the extent of mixing was 82±5.2% (Fig. 4D). We then performed additional experiments to better understand the connection between TCR activation, spreading and segregation of LAT–Dronpa from LAT–PA-mCherry.

Aggregation of PA-mCherry-tagged proteins occurs when the conjugated protein contributes binding interactions (Landgraf et al., 2012). Thus, the development of LAT–LAT segregation during spreading indicated that changes were occurring that allowed LAT molecules to contribute to the observed aggregation; presumably this involves an increase in the local concentration of LAT
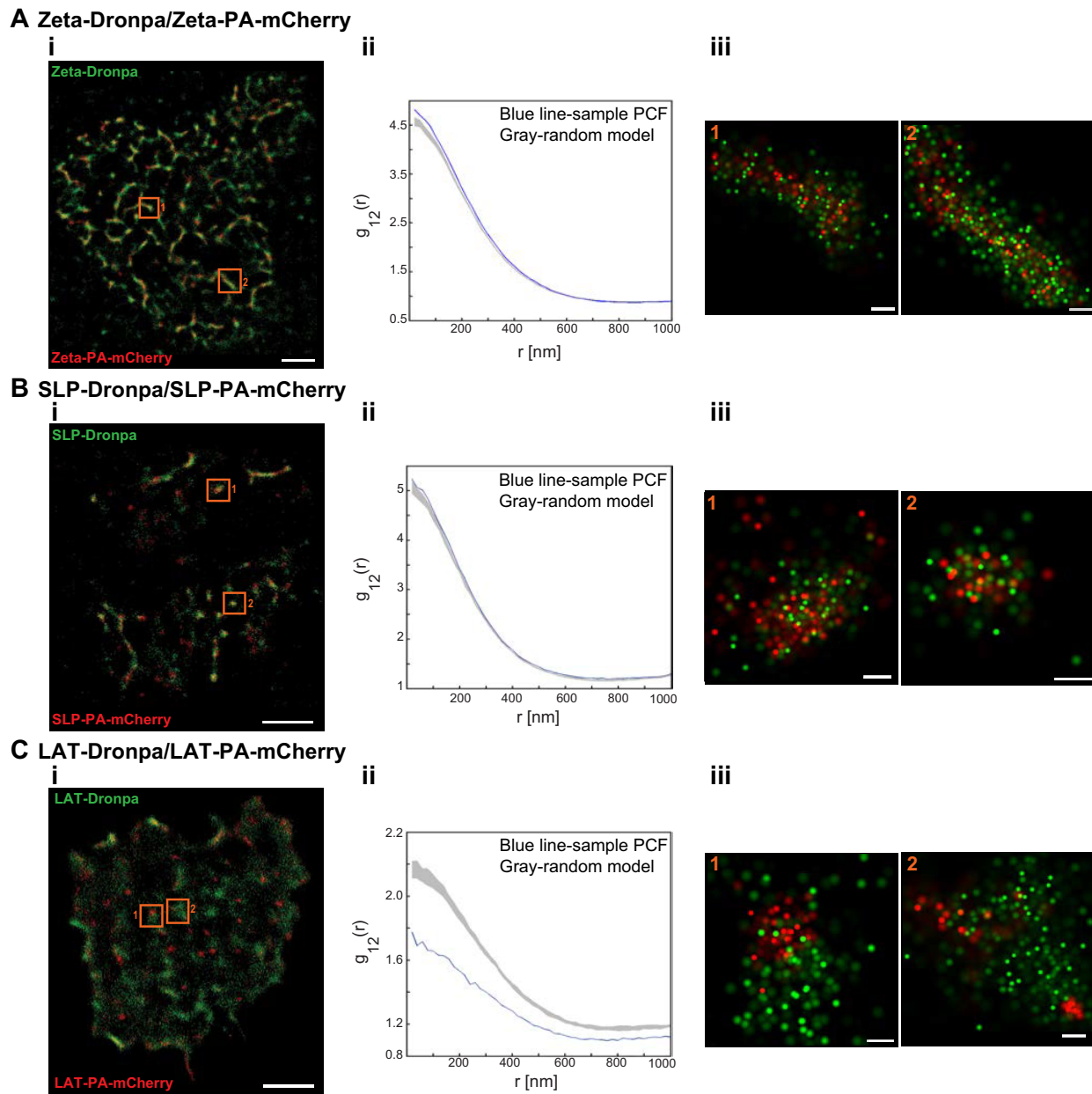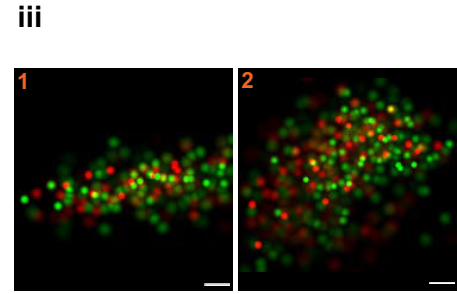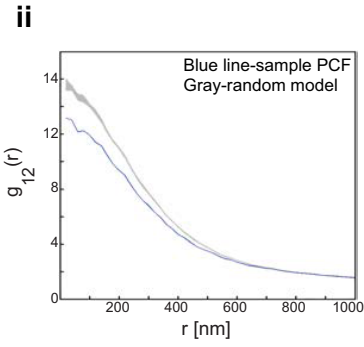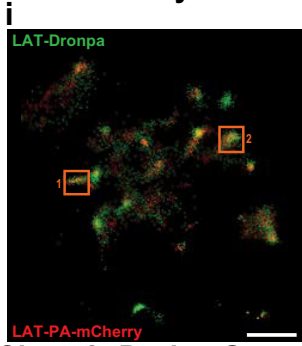
Fig. 3. LAT–Dronpa and LAT–PA–mCherry did not mix well in activated Jurkat T cells. PALM images were obtained of Jurkat T cells expressing two versions of the same protein; one version was conjugated to Dronpa, the other was conjugated to PA-mCherry. (A) Jurkat T cells expressing both TCRζ–Dronpa (zeta-Dronpa) and TCRζ–PA-mCherry (zeta-PA-mCherry) were plated onto stimulatory coverslips and allowed to spread. (i) Rendering of a representative cell showing the localizations of TCRζ–Dronpa (green) and TCRζ–PA-mCherry (red). Maximal values of 1850 molecules/μm² (green) and 1260 molecules/μm² (red). Scale bar: 2 μm. (ii) Bivariate analysis of a central ROI of the same cell. (iii) Renderings of clusters from the same cell, enlarged to show the relationship between TCRζ–Dronpa molecules and TCRζ–PA-mCherry molecules. (iii-1) Maximal values of 5560 molecules/μm² (green) and 3000 molecules/μm² (red). (iii-2) Maximal values of 4030 molecules/μm² (green) and 3350 molecules/μm² (red). Scale bars: 100 nm. (B) Jurkat T cells expressing both SLP–Dronpa and SLP–PA-mCherry were plated onto stimulatory coverslips and allowed to spread. (i) Rendering of a representative cell showing the localizations of SLP–Dronpa (green) and SLP–PA-mCherry (red). Maximal values of 1710 molecules/μm² (green) and 1320 molecules/μm² (red). Scale bar: 2 μm. (ii) Bivariate analysis of a central ROI of the same cell. (iii) Renderings of clusters from the same cell, enlarged to show the relationship between SLP–Dronpa molecules and SLP–PA-mCherry molecules. (iii-1) Maximal values of 4110 molecules/μm² (green) and 2490 molecules/μm² (red). (iii-2) Maximal values of 5570 molecules/μm² (green) and 3500 molecules/μm² (red). Scale bars: 100 nm. (C) Jurkat T cells expressing both LAT–Dronpa and LAT–PA-mCherry were plated onto stimulatory coverslips and allowed to spread. (i) Rendering of a representative cell showing the localizations of LAT–Dronpa (green) and LAT–PA-mCherry (red). Maximal values of 2070 molecules/μm² for (green) and 1480 molecules/μm² (red). Scale bar: 2 μm. (ii) Bivariate analysis of a central ROI of the same cell. (iii) Renderings of clusters from the same cell, enlarged to show the relationship between LAT–Dronpa molecules and LAT–PA-mCherry molecules. (iii-1) Maximal values of 2190 molecules/μm² (green) and 2400 molecules/μm² (red). (iii-2) Maximal values of 3170 molecules/μm² (green) and 1320 molecules/μm² (red). Scale bars: 100 nm.
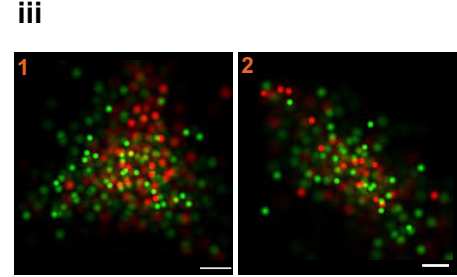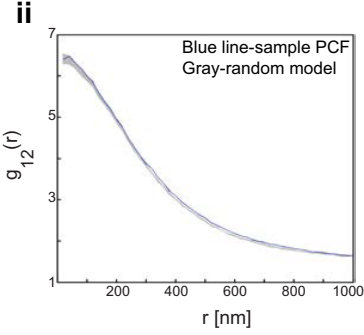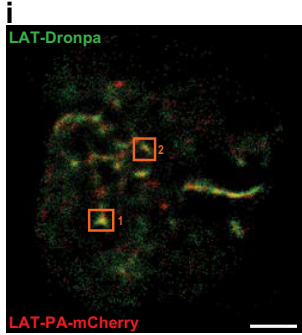
molecules that allowed weak interactions between LAT molecules to amplify the weak association of PA-mCherry modules. This could, in part, reflect the oligomerization of LAT induced by activation, but intrinsic properties of LAT might also be important.

As LAT has been reported to preferentially associate with ordered membrane domains (Janes et al., 1999; Kabouridis, 2006), we sought to disrupt the segregation of LAT–Dronpa and LAT–PA-mCherry by changing the membrane domain structure. First, we
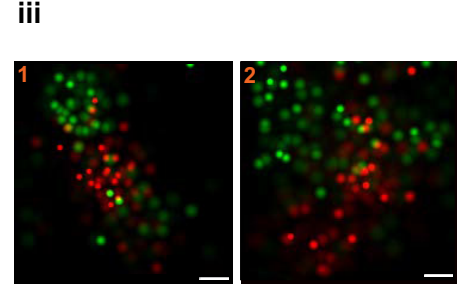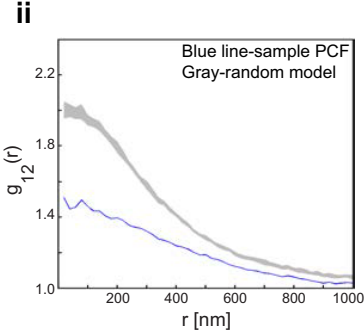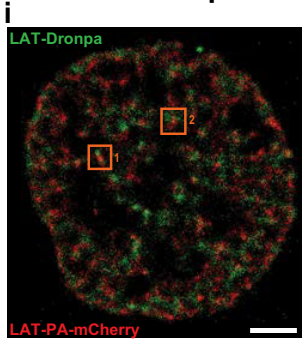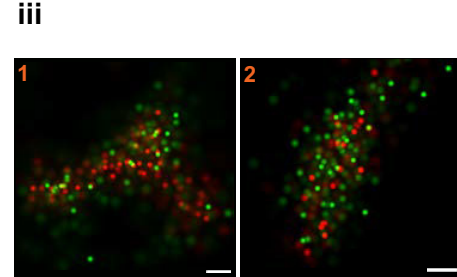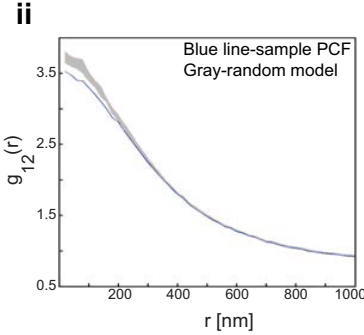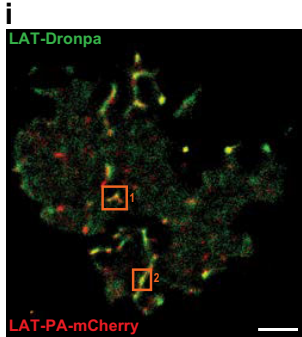
Fig. 4. See next page for legend.

Fig. 4. Segregation of LAT–Dronpa and LAT–PA-mCherry was seen only in well-spread Jurkat T cells and required TCR engagement. (A–C) PALM images were obtained of Jurkat T cells expressing LAT–Dronpa and LAT–PA-mCherry at various times after activation. (A) LAT–Dronpa and LAT–PA-mCherry were well mixed in Class 1 cells. (i) Rendering of a representative cell showing the localizations of LAT–Dronpa (green) and LAT–PA-mCherry (red). Maximal values of 1660 molecules/μm^2 (green) and 12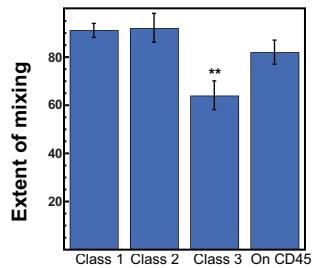40 molecules/μm^2 (red). Scale bar: 2 μm. (ii) Bivariate analysis of a central ROI of the same cell. (iii) Renderings of clusters from the same cell, enlarged to show the relationship between LAT–Dronpa molecules and LAT–PA-mCherry molecules. (iii-1) Maximal values of 1280 molecules/μm^2 (green) and 1270 molecules/μm^2 (red). (iii-2) Maximal values of 1920 molecules/μm^2 (green) and 1420 molecules/μm^2 (red). Scale bars: 100 nm. (B) LAT–Dronpa and LAT–PA-mCherry were also well mixed in Class 2 cells. (i) Rendering of a representative cell showing the localizations of LAT–Dronpa (green) and LAT–PA-mCherry (red). Maximal values of 1580 molecules/μm^2 (green) and 1170 molecules/μm^2 (red). Scale bar: 2 μm. (ii) Bivariate analysis of a central ROI of the same cell. (iii) Renderings of enlarged clusters from the same cell. (iii-1) Maximal values of 4030 molecules/μm^2 (green) and 2320 molecules/μm^2 (red). (iii-2) Maximal values of 2410 molecules/μm^2 (green) and 1900 molecules/μm^2 (red). Scale bars: 100 nm. (C) LAT–Dronpa and LAT–PA-mCherry were segregated in the well-spread Class 3 cells. (i) Rendering of a representative cell showing the localizations of LAT–Dronpa (green) and LAT–PA-mCherry (red). Maximal values of 1260 molecules/μm^2 (green) and 800 molecules/μm^2 (red). Scale bar: 2 μm. (ii) Bivariate analysis of a central ROI of the same cell. (iii) Renderings of enlarged clusters from the same cell. (iii-1) Maximal values of 1750 molecules/μm^2 (green) and 2040 molecules/μm^2 (red). (iii-2) Maximal values of 2010 molecules/μm^2 (green) and 1490 molecules/μm^2 (red). Scale bars: 100 nm. (D) No segregation was seen between LAT–Dronpa and LAT–PA-mCherry in cells plated on a non-stimulatory coverslip coated with anti-CD45 antibodies. (i) Rendering of a representative cell showing the localizations of LAT–Dronpa (green) and LAT–PA-mCherry (red). Maximal values of 1810 molecules/μm^2 (green) and 1460 molecules/μm^2 (red). Scale bar: 2 μm. (ii) Bivariate analysis of a central ROI of the same cell. (iii) Renderings of enlarged clusters from the same cell. (iii-1) Maximal values of 2910 molecules/μm^2 (green) and 2510 molecules/μm^2 (red). (iii-2) Maximal values of 4440 molecules/μm^2 (green) and 3050 molecules/μm^2 (red). Scale bars: 100 nm. (E) Overall extent of mixing. Bars show s.e.m. Class 1, $n=8$ (four experiments); Class 2, $n=20$ (seven experiments); Class 3, $n=22$ (four experiments); plated on CD45 (four experiments), $n=20$. **$P<0.001$ between Class 1 and Class 3 (two-tailed Student's t-test with unequal variance).

treated transfected Jurkat T cells with lidocaine, which disrupts ordered domains and increases membrane fluidity (Park et al., 2012). This produced an increase in the mixing of LAT–Dronpa and LAT–PA-mCherry that was evident in the rendering of a representative cell (Fig. 5Ai), the bivariate analysis (Fig. 5Aii) and representative clusters (Fig. 5Aiii). The overall extent of mixing was 77±5.4%, whereas the extent of mixing in vehicle-treated cells was 70±5.7% (Fig. 5C). Next, we plated the cells at 39°C, which should produce a greater increase in membrane fluidity (Katkere et al., 2010). This treatment restored uniform mixing of LAT molecules as seen in the whole-cell rendering (Fig. 5Bi), bivariate curve (Fig. 5Bii) and renderings of individual clusters (Fig. 5Biii). The extent of mixing increased to 84±4.5%, which was significantly different from the extent of mixing in cells plated at 37°C of 63±5.7% ($P=0.007$, two-tailed Student's t-test) (Fig. 5C). This suggested that the segregation of LAT–Dronpa and LAT–PA-mCherry required the partitioning of LAT molecules into phase-separated membrane domains and also indicated that this partitioning occurred during T cell activation.

However, LAT molecules conjugated to fluorophores that show very little self-association should not segregate even if the local concentration of LAT increases. Neither Dronpa nor PA-GFP form aggregates in the Clp assay (Wang et al., 2014a). Therefore, we examined the mixing of LAT–Dronpa with LAT–PA-GFP. Imaging

of two proteins with similar spectral characteristics is challenging (Fig. S2) (see Materials and Methods) (Sherman et al., 2016). We used two properties to differentiate between these fluorescent proteins. First, Dronpa emissions were separated from those of PA-GFP because Dronpa can be activated with low-energy 340-nm light that does not activate PA-GFP (Sherman et al., 2016). Higher energy 340-nm light was used to photobleach Dronpa molecules without affecting PA-GFP. Dronpa fluorescence also decays more rapidly that PA-GFP. Delaying the onset of image capture after activation provided additional assurance that no Dronpa molecules were captured in the PA-GFP images. We found that LAT–PA-GFP and LAT–Dronpa were well mixed even in the well-spread Class 3 cells (Fig. 6A) with a high overall extent of mixing of 87±5.0%. In cells plated onto a non-stimulatory surface coated with anti-CD45 antibodies (Fig. 6B), the extent of mixing was similar at 90±4.6%, so activation did not cause segregation of LAT–Dronpa from LAT–PA-GFP. Interestingly, the choice of fluorophore had little effect on the size of LAT nanoclusters as determined by nearest neighbor analysis (Fig. S3); that is, even LAT conjugated to PA-mCherry did not form significantly larger clusters. So whereas LAT–PA-mCherry clusters were more stable and exchanged less with other LAT molecules, they did not appear to increase in size.

We could now re-examine the LAT–SLP-76 nanostructure using LAT–PA-GFP and SLP–Dronpa. These two conjugated proteins were well mixed at first, but separated from each other in well-spread cells (Fig. 7A–C). The extent of mixing showed a drop in the well-spread Class 3 cells, going from 87±2.6% in Class 1 and 79.5±3.3% in Class 2 down to 67±3.6%. In addition, in individual clusters, SLP–Dronpa was seen on the outside of the LAT–PA-GFP clusters (Fig. 7Ciii). Once again, this structure required an intact actin cytoskeleton (Fig. 7D). In Latrunculin-A-treated cells, the extent of mixing was 83±3.9%. Overall, these results showed that late in the spreading process, signaling clusters in T cells developed nanostructure characterized by the segregation of LAT and SLP-76 with SLP-76 molecules preferentially located on the outside of LAT clusters. An active actin cytoskeleton was involved in arranging these molecules. This pattern was detected more easily when SLP-76 was conjugated to PA-mCherry because, presumably, the self-aggregation of PA-mCherry helped to stabilize this structure. However, it clearly developed even in the absence of a contribution from the fluorescent protein used in the chimeric construct.

DISCUSSION

We have shown a change in the molecular structure of LAT-based signaling complexes over time. When signaling complexes form on the surface of T cells, LAT and SLP-76 are well mixed; however, once the T cell has completely spread, SLP-76 molecules are preferentially located at the edges of LAT clusters. This nanostructure develops well after the initial phosphorylation of both proteins and Ca^{2+} flux, but well before late events, such as gene transcription, begin in the activated T cell. An intact actin cytoskeleton is required for this re-organization of molecules. This requirement is highlighted by the fact that LAT–SLP-76 nanostructure also fails to develop in cells where the link between SLP-76 and actin polymerization is disrupted by mutation of crucial tyrosine residues (Wu et al., 1996; Wunderlich et al., 1999) that provide binding sites for Vav and Nck (Sherman et al., 2011). Finally, as multiple proteins are brought to the clusters by SLP-76 and their cooperative interactions with one another are needed for stable complex formation, the visualization of LAT–SLP-76 structure implies that other proteins might be organized around LAT nanoclusters.
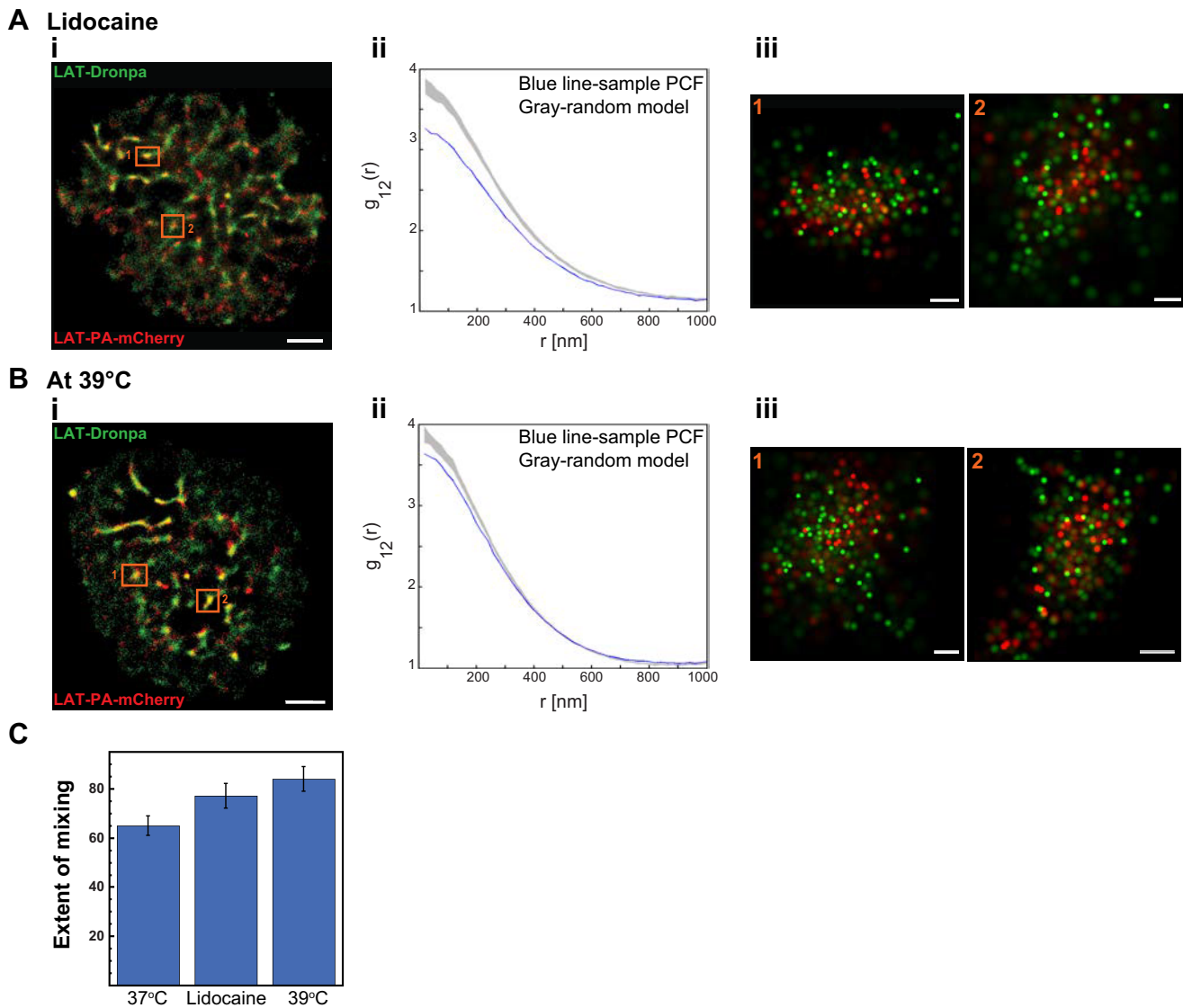
Fig. 5. Segregation of LAT–Dronpa and LAT–PA-mCherry decreased as membrane fluidity increased. PALM images were obtained of Jurkat T cells expressing LAT–Dronpa and LAT–PA-mCherry after activation. (A) LAT–Dronpa and LAT–PA-mCherry showed increased mixing in cells treated with lidocaine, even in Class 3 cells. (i) Rendering of a representative cell showing the localizations of LAT–Dronpa (green) and LAT–PA-mCherry (red). Maximal values of 1780 molecules/μm^2 (green) and 1150 molecules/μm^2 (red). Scale bar: 2 μm. (ii) Bivariate analysis of a central ROI of the same cell. (iii) Renderings of clusters from the same cell, enlarged to show the relationship between LAT–Dronpa molecules and LAT–PA-mCherry molecules. (iii-1) Maximal values of 3480 molecules/μm^2 (green) and 2410 molecules/μm^2 (red). (iii-2) Maximal values of 2670 molecules/μm^2 (green) and 2040 molecules/μm^2 (red). Scale bars: 100 nm. (B) LAT–Dronpa and LAT–PA-mCherry were well mixed in cells equilibrated and plated at 39°C, even in Class 3 cells. (i) Rendering of a representative cell showing the localizations of LAT–Dronpa (green) and LAT–PA-mCherry (red). Maximal values of 1960 molecules/μm^2 (green) and 1170 molecules/μm^2 (red). Scale bar: 2 μm. (ii) Bivariate analysis of a central ROI of the same cell. (iii) Renderings of enlarged clusters from the same cell. (iii-1) Maximal values of 3110 molecules/μm^2 (green) and 2370 molecules/μm^2 (red). (iii-2) Maximal values of 5560 molecules/μm^2 (green) and 3600 molecules/μm^2 (red). Scale bars: 100 nm. (C) Overall extent of mixing. Bars show s.e.m. 37°C, n=22 (four experiments), Lidocaine: n=10 (four experiments), 39°C, n=23 (four experiments).

Nanoscale organization could develop in several different ways. The patterning of LAT and SLP-76 might be associated with crosslinking of LAT by Grb2 and Sos1 (Houtman et al., 2006; Kortum et al., 2013). Grb2 binds to the same phosphorylation sites used by Gads, so SLP-76 might be excluded from areas where oligomerized LAT is bound to Grb2. In addition, crosslinking of SLP-76 by ADAP (Coussens et al., 2013) could help segregate LAT and SLP-76 if the two populations of oligomers (LAT–Grb2-Sos1 and SLP-76-ADAP) are unable to mix. Another possible mechanism depends on the interaction of SLP-76 with Vav and Nck, which provides an indirect link to actin fibers through the Nck-binding protein WASP and Arp2/3 (Krause et al., 2000; Zeng et al.,

2003). Actin polymerization might then pull these SLP-76 molecules to the edges of LAT clusters. This would help explain why the LAT–SLP-76 nanostructure fails to develop in cells lacking the tyrosine residues that bind to Vav and Nck (Sherman et al., 2011). This effect could be further enhanced by differential internalization of SLP-76 molecules bound to different proteins (Clements, 2003). If the SLP-76 molecules that are restricted to the periphery of LAT clusters by interactions with actin mediated by Vav and Nck are also resistant to internalization, while SLP-76 molecules interacting with other proteins are removed from LAT clusters by endocytosis (Barr et al., 2006), the result would be a loss of SLP-76 molecules everywhere except the edges of LAT clusters.
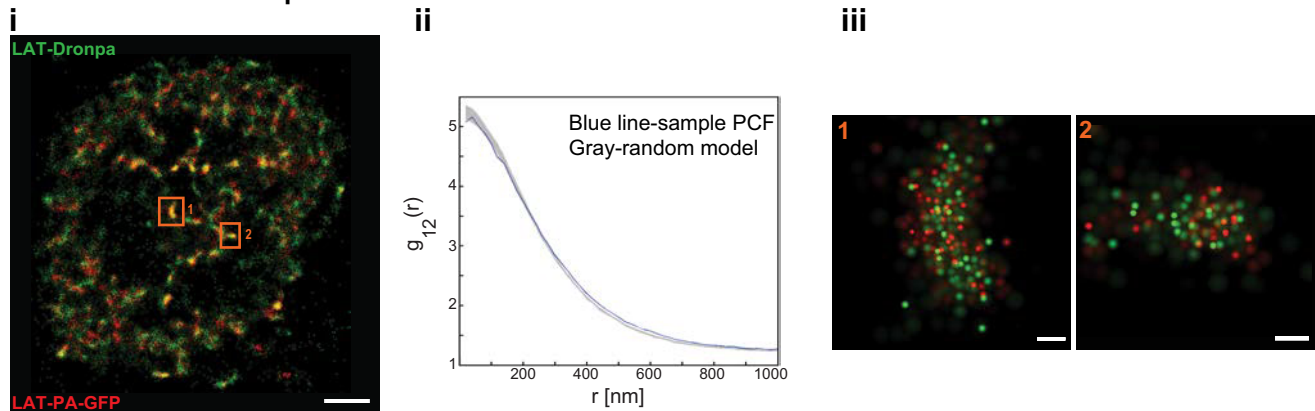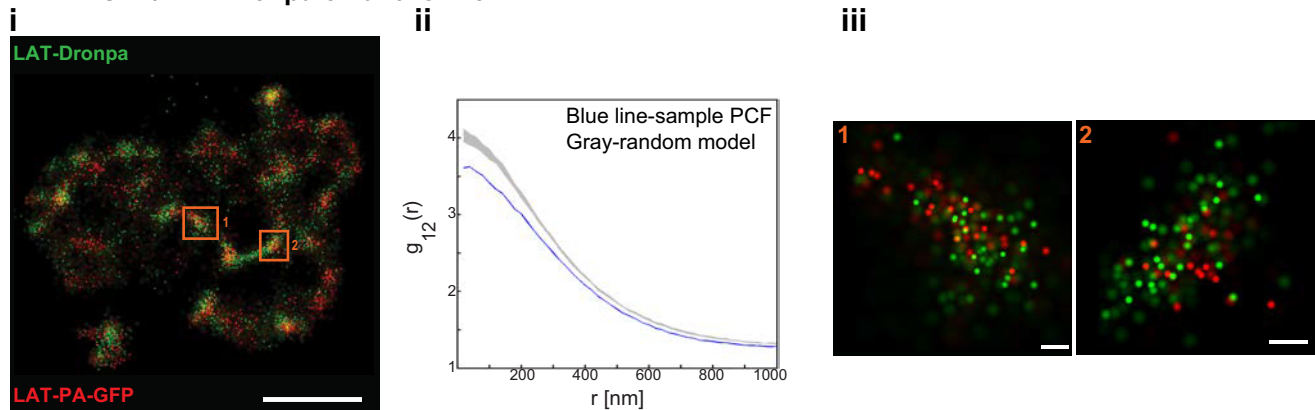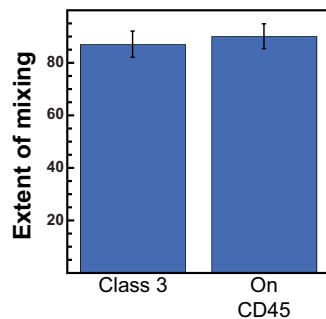
Fig. 6. LAT–Dronpa and LAT–PA-GFP mixed equally in well-spread Jurkat T cells in the presence and absence of TCR engagement. PALM images were obtained of Jurkat T cells expressing LAT–Dronpa and LAT–PA-GFP. (A) LAT–Dronpa and LAT–PA-GFP were well mixed in well-spread cells plated on a stimulatory coverslip. (i) Rendering of a representative cell showing the localizations of LAT (green) and LAT–PA-GFP (red). Maximal values of 1610 molecules/μm^2 (green) and 1180 molecules/μm^2 (red). Scale bar: 2 μm. (ii) Bivariate analysis of a central ROI of the same cell. (iii) Renderings of clusters from the same cell, enlarged to show the relationship between LAT–Dronpa molecules and LAT–PA-GFP molecules. (iii-1) Maximal values of 4170 molecules/μm^2 (green) and 4690 molecules/μm^2 (red). (iii-2) Maximal values of 3150 molecules/μm^2 (green) and 3160 molecules/μm^2 (red). Scale bars: 100 nm. (B) LAT–Dronpa and LAT–PA-GFP were well mixed in cells plated on a non-stimulatory coverslip coated with anti-CD45 antibodies. (i) Rendering of a representative cell showing the localizations of LAT–Dronpa (green) and LAT–PA-GFP (red). Maximal values of 1440 molecules/μm^2 (green) and 940 molecules/μm^2 (red). Scale bar: 2 μm. (ii) Bivariate analysis of a central ROI of the same cell. (iii) Renderings of enlarged clusters from the same cell. (iii-1) Maximal values of 2980 molecules/μm^2 (green) and 2330 molecules/μm^2 (red). (iii-2) Maximal values of 3190 molecules/μm^2 (green) and 3030 molecules/μm^2 (red). Scale bars: 100 nm. (C) Overall extent of mixing. Bars show s.e.m. Class 3, n=14 (two experiments); plated on CD45, n=5 (one experiment).

LAT–SLP nanostructure could also be linked to changes in the domain structure of the T cell plasma membrane. The properties of PA-mCherry allowed us to detect an increased association of LAT molecules with themselves that is also seen only in well-spread cells. The separation of LAT–PA-mCherry from LAT–Dronpa indicates increased interactions between LAT molecules, suggesting that the local concentration of LAT increases late in the spreading process. This LAT–LAT interaction is perturbed by increased membrane fluidity, which is interesting as LAT tends to associate with ordered membrane domains (Kabouridis, 2006). One possibility is that ordered domains containing LAT tend to coalesce in well-spread cells, producing areas of closely packed LAT molecules. These larger domains might account for modest increases in the size of LAT clusters following activation as well as development of nanostructure. It is possible that LAT molecules bound to SLP-76 tend to be excluded from these ordered domains thus separating them from domain-
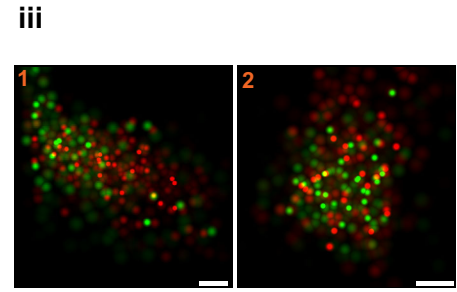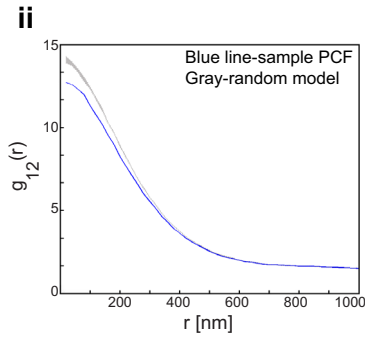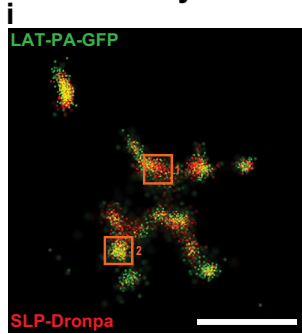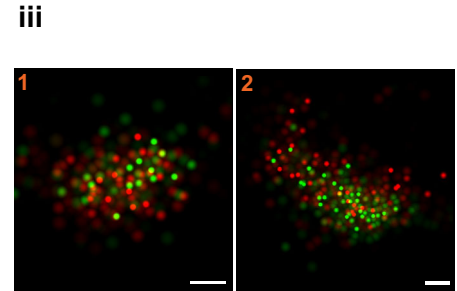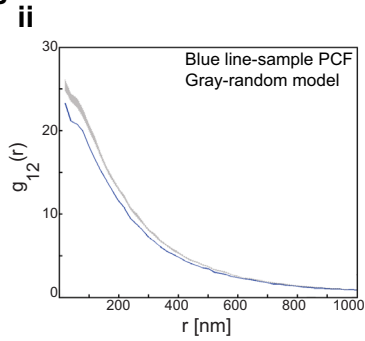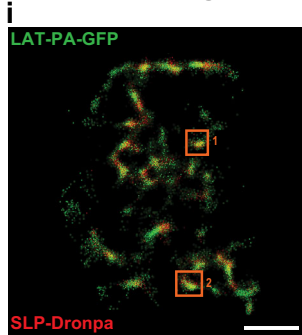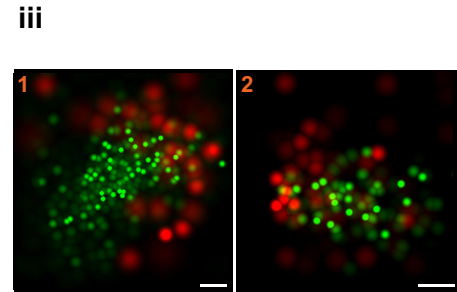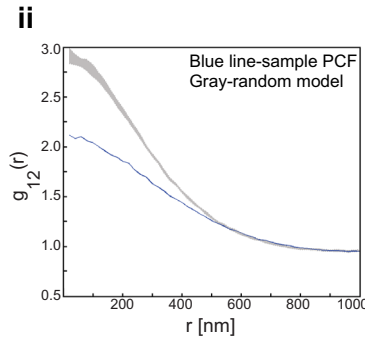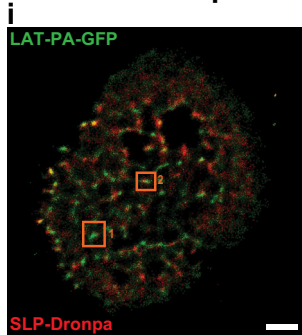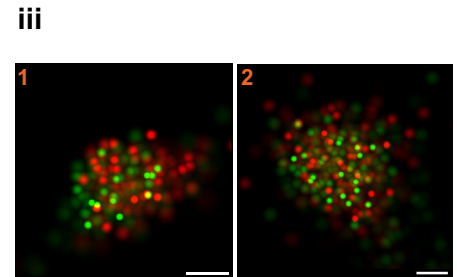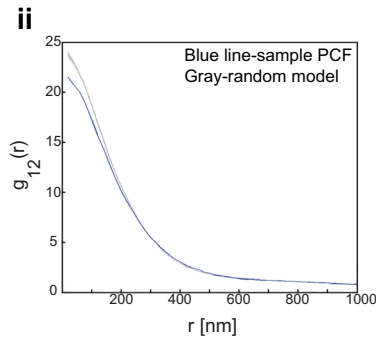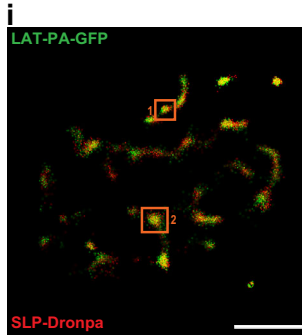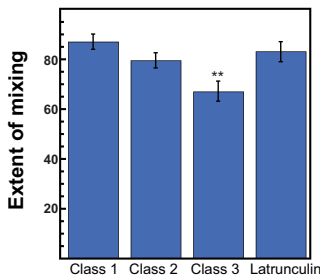
Fig. 7. See next page for legend.

Fig. 7. LAT–SLP-76 nanostructure developed in Jurkat T cells expressing LAT–PA-GFP and SLP–Dronpa. PALM images were obtained of Jurkat T cells expressing LAT–PA-GFP and SLP–Dronpa. (A) LAT–PA-GFP and SLP–Dronpa were well mixed in Class 1 cells. (i) Rendering of a representative cell showing the localizations of LAT–PA-GFP (green) and SLP–Dronpa (red). Maximal values of 1830 molecules/μm^2 (green) and 1890 molecules/μm^2 (red). Scale bar: 2 μm. (ii) Bivariate analysis of a central ROI of the same cell. (iii) Renderings of clusters from the same cell, enlarged to show the relationship between LAT–PA-GFP molecules and SLP–Dronpa molecules. (iii-1) Maximal values of 2700 molecules/μm^2 (green) and 3880 molecules/μm^2 (red). (iii-2) Maximal values of 4980 molecules/μm^2 (green) and 3700 molecules/μm^2 (red). Scale bars: 100 nm. (B) LAT–PA-GFP and SLP–Dronpa were well mixed in Class 2 cells. (i) Rendering of a representative cell showing the localizations of LAT–PA-GFP (green) and SLP–Dronpa (red). Maximal values of 1390 molecules/μm^2 (green) and 2130 molecules/μm^2 (red). Scale bar: 2 μm. (ii) Bivariate analysis of a central ROI of the same cell. (iii) Renderings of enlarged clusters from the same cell. (iii-1) Maximal values of 3810 molecules/μm^2 (green) and 3330 molecules/μm^2 (red). (iii-2) Maximal values of 3630 molecules/μm^2 (green) and 3130 molecules/μm^2 (red). Scale bars: 100 nm. (C) LAT–PA-GFP and SLP–Dronpa were segregated in the well-spread Class 3 cells. (i) Rendering of a representative cell showing the localizations of LAT–PA-GFP (green) and SLP–Dronpa (red). Maximal values of 1670 molecules/μm^2 (green) and 890 molecules/μm^2 (red). Scale bar: 2 μm. (ii) Bivariate analysis of a central ROI of the same cell. (iii) Renderings of enlarged clusters from the same cell. (iii-1) Maximal values of 2590 molecules/μm^2 (green) and 430 molecules/μm^2 (red). (iii-2) Maximal values of 2420 molecules/μm^2 (green) and 930 molecules/μm^2 (red). Scale bars: 100 nm. (D) LAT–PA-GFP and SLP–Dronpa were well mixed in cells treated with Latrunculin A. (i) Rendering of a representative cell showing the localizations of LAT–PA-GFP (green) and SLP–Dronpa (red). Maximal values of 2080 molecules/μm^2 (green) and 1850 molecules/μm^2 (red). Scale bar: 2 μm. (ii) Bivariate analysis of a central ROI of the same cell. (iii) Renderings of enlarged clusters from the same cell, enlarged to show the relationship between LAT–PA-GFP molecules and SLP–Dronpa molecules. (iii-1) Maximal values of 4380 molecules/μm^2 (green) and 2860 molecules/μm^2 (red). (iii-2) Maximal values of 3300 molecules/μm^2 (green) and 2390 molecules/μm^2 (red). Scale bars: 100 nm. (E) Overall extent of mixing. Bars show s.e.m. Class 1, n=32 (six experiments); Class 2, n=24 (six experiments); Class 3, n=23 (six experiments); Latrunculin A treated, n=15 (two experiments). *P<0.001 between Class 1 and Class 3 (two-tailed Student's t-test with unequal variance); no significant difference between Class1 and Class 2, or Class 1 and Latrunculin-A-treated cells.

associated LAT molecules. LAT bound to SLP-76 would then remain on the outside or borders of the domains, producing the LAT–SLP-76 nanostructure we observed. Recent experiments on *in vitro* reconstitution of TCR signaling have demonstrated the importance of phase transitions in proximal phosphorylation events and signal transduction (Su et al., 2016). Perhaps phase transitions or changes in membrane ordering occur throughout the spreading process and help determine which signaling pathways become activated.

Actin is required for the development of nanoscale LAT–SLP-76 organization and LAT–LAT segregation. The late timing indicates that this is different from the very dynamic actin involved in cell spreading or retrograde flow at the edges of the cell. Loss of the actin cytoskeleton would affect all of our proposed models of nanostructure development. If SLP-76 at the edges of LAT clusters is attached to actin filaments through Nck or WASP, the loss of actin structure would disrupt pattern formation. Alternatively, stable actin corrals (Kusumi et al., 2012) could be needed to maintain membrane domains, as indicated by recent work showing the importance of the actin cytoskeleton in maintaining CD1d nanoclusters on APCs (Torreno-Pina et al., 2016). Removing actin would perturb the development of ordered membrane patches, leading to the loss of LAT–SLP-76 organization.

We have also noted that the structural analysis of protein complexes using PALM imaging is complicated by the contribution

that fluorescent proteins themselves might add to protein–protein interactions. Our earlier study using LAT–Dronpa and SLP–PA-mCherry found a significantly greater segregation of those two proteins in well-spread Jurkat T cells (Sherman et al., 2011) than we found here. Those earlier results were likely due to a combination of the intrinsic separation of LAT and SLP-76 augmented by the tendency for PA-mCherry to oligomerize. In this study, we determined that the LAT–SLP-76 organization does not require a contribution from PA-mCherry oligomerization by using fluorescent protein conjugates that do not enhance protein–protein interactions. Dronpa and PA-GFP do not induce aggregation even when conjugated to a test protein known to produce self-association in other fluorescent proteins (Wang et al., 2014a). Nonetheless, LAT–PA-GFP and SLP–Dronpa show segregation and development of nanostructure in well-spread cells. In another study, we determined that the extent of misidentification of Dronpa and PA-GFP was less than 2%, which should have little effect on the bivariate statistics used to analyze the PALM images (Sherman et al., 2016, 2013). The observed segregation of LAT–PA-GFP and SLP–Dronpa is further evidence for the success of this approach as misidentification of emissions would be expected to result in randomization and the loss of the pattern seen here. Furthermore, the experiments on LAT–LAT interactions indicate that the judicious use of self-aggregating fluorescent protein tags could aid in the study of weak protein–protein interactions *in vivo* and the effect of membrane organization on these interactions.

These results strongly suggest that there are different kinds of LAT-based complexes. Those at the center of clusters do not bind SLP-76; however, earlier work has shown that LAT molecules throughout the clusters can bind Grb2 (Sherman et al., 2011). Therefore, it is likely that central LAT molecules are bound to other effectors that compete with SLP-76 binding, perhaps activating other signaling pathways.

A large number of membrane proteins are organized in nanoclusters (Garcia-Parajo et al., 2014); consequently, changes in nanostructure could be important in many processes. Nanoclustering might be involved in both the activation and regulation of signaling pathways. Recent work has suggested a role for nanoclusters in both EGF receptor signaling (Wang et al., 2014b) and neural circuits (Broadhead et al., 2016). The nanoclustering of H-Ras has a direct effect on specific Raf effector recruitment (Guzman et al., 2014). We have now documented changes in the molecular organization of signaling complexes following TCR stimulation. The nanoscale organization of LAT-based complexes is dynamic not static; these changes might be required for temporal control of the many different signaling outputs required for T cell activation.

MATERIALS AND METHODS
Cell tissue culture and inhibitor treatments
Wild-type (E6.1) Jurkat T cells (ATCC, Manassas, VA; checked for mycoplasm on 24 Jun 2014) were maintained in RPMI 1640 supplemented with 10% fetal bovine serum and antibiotics. Tissue culture reagents were from Gibco-ThermoFisher (Grand Island, NY).

Cells were incubated in 300 nM Latrunculin A (Invitrogen-ThermoFisher, Grand Island, NY) for a total of 5 min. Lidocaine was obtained from Sigma-Aldrich (St Louis, MO) and was used at 150 μM, with a 10-min pre-incubation. Inhibitors were present throughout cell plating and incubation with coverslips.

Plasmids
Proteins tagged with the photoactivatable fluorescent proteins Dronpa (MBL International Corporation, Woburn, MA), PA-mCherry and PA-GFP were generated in EGFP-N1 or EGFP-C1 vectors (Clontech, Mountain

View, CA) as previously described (Bunnell et al., 2002; Sherman et al., 2011).

E6.1 Jurkat T cells were transfected using the LONZA nucleofector shuttle system (Basel Switzerland), program H-10 and the Amaxa T-kit. Transfected cells were maintained in transfection medium [RPMI, 10% fetal calf serum (FCS)] and sorted for positive expression of PA-mCherry or Dronpa chimeras 24 h after transfection. Cells were rested overnight, plated 48 h from transfection and imaged over the next 2 days (Sherman et al., 2011).

Sample preparation
The preparation of coverslips containing gold beads as fiducial markers follows a previously described technique (Bunnell et al., 2003). Clean chambered coverslips were coated with 100-nm gold beads (Microspheres-Nanospheres, Cold Spring, NY) that had been sonicated and diluted ×10 in methanol. Alternatively, when TetraSpeck beads (Invitrogen-ThermoFisher, Grand Island, NY) were used as fiducial markers, the addition of gold beads was omitted. Coverslips were subsequently incubated with stimulatory anti-CD3 (clone Ucht1, cat. no. 555330) or non-stimulatory (anti-CD45, clone H130, cat. no. 555480) antibodies (BD Biosciences, San Jose, CA) at a concentration of 10 µg/ml. Cells were plated and fixed (Bunnell et al., 2003). When used, TetraSpeck beads were added to the samples just before imaging.

Imaging
PALM imaging was performed on a TIRF microscope based on an inverted Nikon TI Eclipse Microscope (Nikon Instruments Inc., Melville, NY) with an iXon DU-888 EMCCD 1024×1024 pixel detector (pixel size of 13 mm). Fiduciary markers (0.1-µm gold particles, Microspheres-Nanospheres or TetraSpec 0.1-µm microspheres, Invitrogen-ThermoFisher) were used to correct drift during an image series and to register localizations from two photoactivatable proteins. PALM images were analyzed with the PeakSelector software 5 for the identification of individual peaks in the frames. Next, peaks were grouped and assigned to individual molecules. Individual molecules are presented in rendered images with intensities that correspond to the probability density values of their fitted Gaussian with respect to the maximal probability density values detected in the field. Peak grouping combined localizations based on a distance threshold and a temporal gap to account for possible molecular blinking (Annibale et al., 2011; Sengupta et al., 2011). A range of temporal gaps were considered for each fluorophore separately. Increasing the temporal gap decreased the number of detected molecules exponentially until a plateau was reached. We chose a gap that reduced the number of detected molecules to within 15% of the plateau value; this was 15 frames for all fluorophores. This procedure minimized the possible over-counting of molecules caused by reactivation or blinking of the fluorescent proteins.

Classifying cells
When a Jurkat T cell first lands on a stimulatory surface, there are usually one or two small areas of contact. Then, there is a brief phase where more contacts appear as more cell protrusions touch the stimulatory surface. During spreading, these contact sites merge together until there is a single surface. The surface then expands radially outward until the cell reaches its full contact and extension. On rare occasions, there might be two surfaces spreading radially at the same time and then they merge near the end of the spreading process. Movie 1 shows an example of a Jurkat T cell expressing LAT–YFP during spreading.

To classify the cells analyzed in Figs 1 and 7, we used TIRF movies of LAT–YFP dynamics to determine rules for classifying cells, dividing this continuous process into three phases: Class 1, first contact; Class 2, spreading; and Class 3, well-spread (Fig. S1A–C). We took snapshots from the movies to develop criteria for classifying the PALM images of fixed cells that were taken at a single timepoint. For analysis of the PALM images, a combined image of the raw data of the entire PALM series of LAT–Dronpa (Fig. 1) or LAT–PA-GFP (Fig. 7) was used to determine the area of the LAT footprint and the number of contact points.

We determined the total area of LAT fluorescence in single images taken from the TIRF movies to see if we could separate cells into our three classes

using the surface creation feature of Imaris (Bitplane, Concord, MA) to measure the fluorescence area. However, the range in the size of Jurkat T cells and variations in cell spreading allowed us to make only three unambiguous determinations. We concluded that all cells with small areas of LAT fluorescence, those with total areas below 38 µm^2, were always Class 1 cells that had just contacted the stimulatory surface. Furthermore, no Class 1 cell had a total area of LAT fluorescence greater than 120 µm^2. Also, no Class 3 cell or fully spread cell had a total area of LAT fluorescence less than 120 µm^2. Thus, we identified some of the Class 1 cells and determined that there was no overlap between Class 1 and Class 3 cells using the total area of LAT fluorescence.

This left us with two groups of cells that had not been fully classified. Cells with LAT fluorescence areas between 38 µm^2 and 120 µm^2 were a mixture of Class 1 and Class 2 cells. Cells with a total area of LAT fluorescence above 120 µm^2 were a mixture of Class 2 and Class 3 cells. Therefore, we sought additional criteria to separate these cells into classes.

Further examination of the TIRF movies showed that for cells with a total area of LAT fluorescence between 38 µm^2 and 120 µm^2 (the mixture of Class 1 and Class 2 cells), the Class 1 cells had many points of contact, whereas the Class 2 cells that had begun spreading had fewer contact points. Therefore, we examined the number of surfaces created during the measurement of LAT fluorescence in these cells. Cells with more than three surfaces were classified as Class 1 cells, cells with no more than three surfaces were classified as Class 2 cells.

Finally, we needed to separate the cells with a total area of LAT fluorescence above 120 µm^2 into Class 2 and Class 3 cells. In well-spread cells, the expansion of the cell across the stimulatory surface creates a distinctive hat-like morphology where the contact surface is always larger than the cell body containing the nucleus (Bunnell et al., 2001). Thus, in Class 3 cells, the area of LAT fluorescence at the activating surface is always larger than the area of the cell body. A brightfield image was taken of each cell at the end of the PALM imaging, focused on the cell body above the stimulatory surface. If the area of LAT fluorescence was at least 1.1 times the area of the cell body in the corresponding brightfield image, cells were classified as Class 3; those with smaller ratios were classified as Class 2 cells.

LAT clusters dissipate relatively rapidly in spread cells (Bunnell et al., 2002; Fig. S1D, Movies 1 and 2) and we did not wish to determine the nanostructure of LAT that was not in microclusters. We examined all of the Class 3 cells to see if there were visible LAT microclusters. Cells without microclusters were not analyzed.

We also needed to avoid cells that had completed spreading and started to retract from the stimulatory surface. Fortunately, the LAT microclusters dissipate before cell retraction begins. Movie 2 shows the dynamics of actin labeled with LifeAct-Neon and LAT–Apple. Loss of LAT clusters occurred in frame 58, 285.5 s after the start of the movie, which begins just as the activated cell begins spreading. Actin retraction begins after the dissipation of LAT clusters at frame 84, 415.5 s after the start of the movie. Eliminating cells without LAT microclusters also insured that retracted cells were not included in the analysis.

Statistical analysis
Regions of interest (ROIs) near the center of the cells were chosen for analysis (Sherman et al., 2011, 2013). Bivariate pair-correlation functions (PCFs) were generated by a previously published algorithm that accounts for edge effects using a pixelized approach (Wiegand and A. Moloney, 2004). The chosen pixel size was 20 nm, matching the PALM resolution. Nearest neighbor analysis was conducted using customized MatLab code (Sherman et al., 2011) with a proximity threshold of 30 nm.

Figure production
Graphs were produced with KaleidaGraph (Synergy Software, Reading, PA). Renderings of PALM images were produced using PeakSelector software 5. These images were made into figures using Photoshop and Illustrator (Adobe Systems Inc., San Jose, CA). Individual images were mounted on black boxes to create panels of uniform size. Scale bars stamped on the images were removed and replaced with bars drawn in Photoshop for improved clarity.

Supplementary information
Supplementary information available online at
http://jcs.biologists.org/lookup/doi/10.1242/jcs.194886.supplemental

References

Allen, J. R., Ross, S. T. and Davidson, M. W. (2013). Single molecule localization microscopy for superresolution. *J. Optics* **15**, 094001.

Annibale, P., Vanni, S., Scarselli, M., Rothlisberger, U. and Radenovic, A. (2011). Identification of clustering artifacts in photoactivated localization microscopy. *Nat. Methods* **8**, 527-528.

Balagopalan, L., Barr, V. A., Sommers, C. L., Barda-Saad, M., Goyal, A., Isakowitz, M. S. and Samelson, L. E. (2007). c-Cbl-mediated regulation of LAT-nucleated signaling complexes. *Mol. Cell. Biol.* **27**, 8622-8636.

Balagopalan, L., Coussens, N. P., Sherman, E., Samelson, L. E. and Sommers, C. L. (2010). The LAT story: a tale of cooperativity, coordination, and choreography. *Cold Spring Harb. Perspect. Biol.* **2**, a005512.

Balagopalan, L., Sherman, E., Barr, V. A. and Samelson, L. E. (2011). Imaging techniques for assaying lymphocyte activation in action. *Nat. Rev. Immunol.* **11**, 21-33.

Balagopalan, L., Kortum, R. L., Coussens, N. P., Barr, V. A. and Samelson, L. E. (2015). The linker for activation of T cells (LAT) signaling hub: from signaling complexes to microclusters. *J. Biol. Chem.* **290**, 26422-26429.

Barda-Saad, M., Braiman, A., Titerence, R., Bunnell, S. C., Barr, V. A. and Samelson, L. E. (2005). Dynamic molecular interactions linking the T cell antigen receptor to the actin cytoskeleton. *Nat. Immunol.* **6**, 80-89.

Barda-Saad, M., Shirasu, N., Pauker, M. H., Hassan, N., Perl, O., Balbo, A., Yamaguchi, H., Houtman, J. C. D., Appella, E., Schuck, P. et al. (2010). Cooperative interactions at the SLP-76 complex are critical for actin polymerization. *EMBO J.* **29**, 2315-2328.

Barr, V. A., Balagopalan, L., Barda-Saad, M., Polishchuk, R., Boukari, H., Bunnell, S. C., Bernot, K. M., Toda, Y., Nossal, R. and Samelson, L. E. (2006). T-cell antigen receptor-induced signaling complexes: internalization via a cholesterol-dependent endocytic pathway. *Traffic* **7**, 1143-1162.

Betzig, E., Patterson, G. H., Sougrat, R., Lindwasser, O. W., Olenych, S., Bonifacino, J. S., Davidson, M. W., Lippincott-Schwartz, J. and Hess, H. F. (2006). Imaging intracellular fluorescent proteins at nanometer resolution. *Science* **313**, 1642-1645.

Boerth, N. J., Judd, B. A. and Koretzky, G. A. (2000). Functional association between SLAP-130 and SLP-76 in Jurkat T cells. *J. Biol. Chem.* **275**, 5143-5152.

Braiman, A., Barda-Saad, M., Sommers, C. L. and Samelson, L. E. (2006). Recruitment and activation of PLCγ1 in T cells: a new insight into old domains. *EMBO J.* **25**, 774-784.

Broadhead, M. J., Horrocks, M. H., Zhu, F., Muresan, L., Benavides-Piccione, R., DeFelipe, J., Fricker, D., Kopanitsa, M. V., Duncan, R. R., Klenerman, D. et al. (2016). PSD95 nanoclusters are postsynaptic building blocks in hippocampus circuits. *Sci. Rep.* **6**, 24626.

Bunnell, S. C., Kapoor, V., Trible, R. P., Zhang, W. G. and Samelson, L. E. (2001). Dynamic actin polymerization drives T cell receptor-induced spreading: a role for the signal transduction adaptor LAT. *Immunity* **14**, 315-329.

Bunnell, S. C., Hong, D. I., Kardon, J. R., Yamazaki, T., McGlade, C. J., Barr, V. A. and Samelson, L. E. (2002). T cell receptor ligation induces the formation of dynamically regulated signaling assemblies. *J. Cell Biol.* **158**, 1263-1275.

Bunnell, S. C., Barr, V. A., Fuller, C. L. and Samelson, L. E. (2003). High-resolution multicolor imaging of dynamic signaling complexes in T cells stimulated by planar substrates. *Sci. STKE* **2003**, pl8.

Campi, G., Varma, R. and Dustin, M. L. (2005). Actin and agonist MHC-peptide complex-dependent T cell receptor microclusters as scaffolds for signaling. *J. Exp. Med.* **202**, 1031-1036.

Clements, J. L. (2003). Known and potential functions for the SLP-76 adapter protein in regulating T-cell activation and development. *Immunol. Rev.* **191**, 211-219.

Coussens, N. P., Hayashi, R., Brown, P. H., Balagopalan, L., Balbo, A., Akpan, I., Houtman, J. C. D., Barr, V. A., Schuck, P., Appella, E. et al. (2013). Multipoint binding of the SLP-76 SH2 domain to ADAP is critical for oligomerization of SLP-76 signaling complexes in stimulated T cells. *Mol. Cell. Biol.* **33**, 4140-4151.

da Silva, A. J., Li, Z., de Vera, C., Canto, E., Findell, P. and Rudd, C. E. (1997). Cloning of a novel T-cell protein FYB that binds FYN and SH2-domain-containing leukocyte protein 76 and modulates interleukin 2 production. *Proc. Natl. Acad. Sci. USA* **94**, 7493-7498.

Endesfelder, U. and Heilemann, M. (2015). Direct Stochastic Optical Reconstruction Microscopy (dSTORM). In *Advanced Fluorescence Microscopy: Methods and Protocols* (ed. J. P. Verveer), pp. 263-276. New York, NY: Springer New York.

Freiberg, B. A., Kupfer, H., Maslanik, W., Delli, J., Kappler, J., Zaller, D. M. and Kupfer, A. (2002). Staging and resetting T cell activation in SMACs. *Nat. Immunol.* **3**, 911-917.

Garcia-Parajo, M. F., Cambi, A., Torreno-Pina, J. A., Thompson, N. and Jacobson, K. (2014). Nanoclustering as a dominant feature of plasma membrane organization. *J. Cell Sci.* **127**, 4995-5005.

Grakoui, A., Bromley, S. K., Sumen, C., Davis, M. M., Shaw, A. S., Allen, P. M. and Dustin, M. L. (1999). The immunological synapse: a molecular machine controlling T cell activation. *Science* **285**, 221-227.

Guzman, C., Solman, M., Ligabue, A., Blazevits, O., Andrade, D. M., Reymond, L., Eggeling, C. and Abankwa, D. (2014). The efficacy of Raf kinase recruitment to the GTPase H-ras depends on H-ras membrane conformer-specific nanoclustering. *J. Biol. Chem.* **289**, 9519-9533.

Heilemann, M., van de Linde, S., Schüttpelz, M., Kasper, R., Seefeldt, B., Mukherjee, A., Tinnefeld, P. and Sauer, M. (2008). Subdiffraction-resolution fluorescence imaging with conventional fluorescent probes. *Angew. Chem. Int. Ed.* **47**, 6172-6176.

Houtman, J. C. D., Yamaguchi, H., Barda-Saad, M., Braiman, A., Bowden, B., Appella, E., Schuck, P. and Samelson, L. E. (2006). Oligomerization of signaling complexes by the multipoint binding of GRB2 to both LAT and SOS1. *Nat. Struct. Mol. Biol.* **13**, 798-805.

Hsu, C.-J. and Baumgart, T. (2011). Spatial association of signaling proteins and F-actin effects on cluster assembly analyzed via photoactivation localization microscopy in T cells. *PLoS ONE* **6**, e23586.

Ilani, T., Vasiliver-Shamis, G., Vardhana, S., Bretscher, A. and Dustin, M. L. (2009). T cell antigen receptor signaling and immunological synapse stability require myosin IIA. *Nat. Immunol.* **10**, 531-539.

Janes, P. W., Ley, S. C. and Magee, A. I. (1999). Aggregation of lipid rafts accompanies signaling via the T cell antigen receptor. *J. Cell Biol.* **147**, 447-461.

Johnson, K. G., Bromley, S. K., Dustin, M. L. and Thomas, M. L. (2000). A supramolecular basis for CD45 tyrosine phosphatase regulation in sustained T cell activation. *Proc. Natl. Acad. Sci. USA* **97**, 10138-10143.

Kabouridis, P. S. (2006). Lipid rafts in T cell receptor signalling (Review). *Mol. Membr. Biol.* **23**, 49-57.

Kaizuka, Y., Douglass, A. D., Varma, R., Dustin, M. L. and Vale, R. D. (2007). Mechanisms for segregating T cell receptor and adhesion molecules during immunological synapse formation in Jurkat T cells. *Proc. Natl. Acad. Sci. USA* **104**, 20296-20301.

Katkere, B., Rosa, S., Caballero, A., Repasky, E. A. and Drake, J. R. (2010). Physiological-range temperature changes modulate cognate antigen processing and presentation mediated by lipid raft-restricted ubiquitinated B cell receptor molecules. *J. Immunol.* **185**, 5032-5039.

Knight, A. E. (2017). Super-resolution fluorescence microscopy, localization microscopy. In *Reference Module in Chemistry, Molecular Sciences and Chemical Engineering, from Encyclopedia of Spectroscopy and Spectrometry (Third Edition)*, pp. 325-330.

Kortum, R. L., Balagopalan, L., Alexander, C. P., Garcia, J., Pinski, J. M., Merrill, R. K., Nguyen, P. H., Li, W., Agarwal, I., Akpan, I. O. et al. (2013). The ability of Sos1 to oligomerize the adaptor protein LAT is separable from its guanine nucleotide exchange activity in vivo. *Sci. STKE* **6**, ra99.

Krause, M., Sechi, A. S., Konradt, M., Monner, D., Gertler, F. B. and Wehland, J. (2000). Fyn-Binding Protein (Fyb)/Slp-76–associated protein (Slap), Ena/Vasodilator-Stimulated Phosphoprotein (Vasp) proteins and the Arp2/3 Complex Link T Cell Receptor (TCR) signaling to the actin cytoskeleton. *J. Cell Biol.* **149**, 181-194.

Krummel, M. F., Sjaastad, M. D., Wulfing, C. and Davis, M. M. (2000). Differential clustering of CD4 and CD3zeta during T cell recognition. *Science* **289**, 1349-1352.

Kusumi, A., Fujiwara, T. K., Morone, N., Yoshida, K. J., Chadda, R., Xie, M., Kasai, R. S. and Suzuki, K. G. N. (2012). Membrane mechanisms for signal transduction: the coupling of the meso-scale raft domains to membrane-skeleton-induced compartments and dynamic protein complexes. *Semin. Cell Dev. Biol.* **23**, 126-144.

Landgraf, D., Okumus, B., Chien, P., Baker, T. A. and Paulsson, J. (2012). Segregation of molecules at cell division reveals native protein localization. *Nat. Methods* **9**, 480-482.

Lee, K.-H., Holdorf, A. D., Dustin, M. L., Chan, A. C., Allen, P. M. and Shaw, A. S. (2002). T cell receptor signaling precedes immunological synapse formation. *Science* **295**, 1539-1542.

Lillemeier, B. F., Mörtelmaier, M. A., Forstner, M. B., Huppa, J. B., Groves, J. T. and Davis, M. M. (2010). TCR and Lat are expressed on separate protein islands on T cell membranes and concatenate during activation. *Nat. Immunol.* **11**, 90-96.

Myung, P. S., Derimanov, G. S., Jordan, M. S., Punt, J. A., Liu, Q.-H., Judd, B. A., Meyers, E. E., Sigmund, C. D., Freedman, B. D. and Koretzky, G. A. (2001). Differential requirement for SLP-76 domains in T cell development and function. *Immunity* **15**, 1011-1026.

Neve-Oz, Y., Razvag, Y., Sajman, J. and Sherman, E. (2015). Mechanisms of localized activation of the T cell antigen receptor inside clusters. *BBA Mol. Cell. Res.* **1853**, 810-821.

Nienhaus, K. and Nienhaus, G. U. (2016). Where do we stand with super-resolution optical microscopy? *J. Mol. Biol.* **428**, 308-322.

Park, J.-S., Jung, T.-S., Noh, Y.-H., Kim, W.-S., Park, W.-I., Kim, Y.-S., Chung, I.-K., Sohn, U. D., Bae, S.-K., Bae, M.-K. et al. (2012). The effect of lidocaine · HCl on the fluidity of native and model membrane lipid bilayers. *Korean J. Physiol. Pharmacol.* **16**, 413-422.

Purbhoo, M. A., Liu, H., Oddos, S., Owen, D. M., Neil, M. A. A., Pageon, S. V., French, P. M. W., Rudd, C. E. and Davis, D. M. (2010). Dynamics of subsynaptic vesicles and surface microclusters at the immunological synapse. *Sci. STKE* **3**, ra36.

Rajasekaran, K., Riese, M. J., Rao, S., Wang, L., Thakar, M. S., Sentman, C. L. and Malarkannan, S. (2016). Signaling in effector lymphocytes: insights toward safer immunotherapy. *Front. Immunol.* **7**, 176.

Rossy, J., Pageon, S. V., Davis, D. M. and Gaus, K. (2013). Super-resolution microscopy of the immunological synapse. *Curr. Opin. Immunol.* **25**, 307-312.

Sengupta, P., Jovanovic-Talisman, T., Skoko, D., Renz, M., Veatch, S. L. and Lippincott-Schwartz, J. (2011). Probing protein heterogeneity in the plasma membrane using PALM and pair correlation analysis. *Nat. Methods* **8**, 969-975.

Sengupta, P., van Engelenburg, S. B. and Lippincott-Schwartz, J. (2014). Superresolution imaging of biological systems using photoactivated localization microscopy. *Chem. Rev.* **114**, 3189-3202.

Sherman, E., Barr, V., Manley, S., Patterson, G., Balagopalan, L., Akpan, I., Regan, C. K., Merrill, R. K., Sommers, C. L., Lippincott-Schwartz, J. et al. (2011). Functional nanoscale organization of signaling molecules downstream of the T cell antigen receptor. *Immunity* **35**, 705-720.

Sherman, E., Barr, V. A. and Samelson, L. E. (2013). Resolving multi-molecular protein interactions by photoactivated localization microscopy. *Methods* **59**, 261-269.

Sherman, E., Barr, V. A., Merrill, R. K., Regan, C. K., Sommers, C. L. and Samelson, L. E. (2016). Hierarchical nanostructure and synergy of multimolecular signalling complexes. *Nat. Commun.* **7**, 12161.

Su, X., Ditlev, J. A., Hui, E., Xing, W., Banjade, S., Okrut, J., King, D. S., Taunton, J., Rosen, M. K. and Vale, R. D. (2016). Phase separation of signaling molecules promotes T cell receptor signal transduction. *Science* **352**, 595-599.

Sydor, A. M., Czymmek, K. J., Puchner, E. M. and Mennella, V. (2015). Super-resolution microscopy: from single molecules to supramolecular assemblies. *Trends Cell Biol.* **25**, 730-748.

Toomre, D. and Manstein, D. J. (2001). Lighting up the cell surface with evanescent wave microscopy. *Trends Cell Biol.* **11**, 298-303.

Torreno-Pina, J. A., Manzo, C., Salio, M., Aichinger, M. C., Oddone, A., Lakadamyali, M., Shepherd, D., Besra, G. S., Cerundolo, V. and Garcia-Parajo, M. F. (2016). The actin cytoskeleton modulates the activation of iNKT cells by segregating CD1d nanoclusters on antigen-presenting cells. *Proc. Natl. Acad. Sci. USA* **113**, E772-E781.

van de Linde, S., Löschberger, A., Klein, T., Heidbreder, M., Wolter, S., Heilemann, M. and Sauer, M. (2011). Direct stochastic optical reconstruction microscopy with standard fluorescent probes. *Nat. Protoc.* **6**, 991-1009.

Varma, R., Campi, G., Yokosuka, T., Saito, T. and Dustin, M. L. (2006). T cell receptor-proximal signals are sustained in peripheral microclusters and terminated in the central supramolecular activation cluster. *Immunity* **25**, 117-127.

Wang, S., Moffitt, J. R., Dempsey, G. T., Xie, X. S. and Zhuang, X. (2014a). Characterization and development of photoactivatable fluorescent proteins for single-molecule–based superresolution imaging. *Proc. Natl. Acad. Sci. USA* **111**, 8452-8457.

Wang, Y., Gao, J., Guo, X., Tong, T., Shi, X., Li, L., Qi, M., Wang, Y., Cai, M., Jiang, J. et al. (2014b). Regulation of EGFR nanocluster formation by ionic protein-lipid interaction. *Cell Res.* **24**, 959-976.

Wiegand, T. and A. Moloney, K. (2004). Rings, circles, and null-models for point pattern analysis in ecology. *Oikos* **104**, 209-229.

Wu, J., Motto, D. G., Koretzky, G. A. and Weiss, A. (1996). Vav and SLP-76 interact and functionally cooperate in IL-2 gene activation. *Immunity* **4**, 593-602.

Wunderlich, L., Faragó, A., Downward, J. and Buday, L. (1999). Association of Nck with tyrosine-phosphorylated SLP-76 in activated T lymphocytes. *Eur. J. Immunol.* **29**, 1068-1075.

Yablonski, D., Kuhne, M. R., Kadlecek, T. and Weiss, A. (1998). Uncoupling of nonreceptor tyrosine kinases from PLC-gamma1 in an SLP-76-deficient T cell. *Science* **281**, 413-416.

Yokosuka, T. and Saito, T. (2010). The immunological synapse, TCR microclusters, and T cell activation. In *Immunological Synapse* (ed. T. Saito and D. F. Batista), pp. 81-107. Berlin; Heidelberg: Springer Berlin Heidelberg.

Yokosuka, T., Sakata-Sogawa, K., Kobayashi, W., Hiroshima, M., Hashimoto-Tane, A., Tokunaga, M., Dustin, M. L. and Saito, T. (2005). Newly generated T cell receptor microclusters initiate and sustain T cell activation by recruitment of Zap70 and SLP-76. *Nat. Immunol.* **6**, 1253-1262.

Zeng, R., Cannon, J. L., Abraham, R. T., Way, M., Billadeau, D. D., Bubeck-Wardenberg, J. and Burkhardt, J. K. (2003). SLP-76 coordinates Nck-dependent Wiskott-Aldrich syndrome protein recruitment with Vav-1/Cdc42-dependent Wiskott-Aldrich syndrome protein activation at the T cell-APC contact site. *J. Immunol.* **171**, 1360-1368.

Zhang, W., Irvin, B. J., Trible, R. P., Abraham, R. T. and Samelson, L. E. (1999a). Functional analysis of LAT in TCR-mediated signaling pathways using a LAT-deficient Jurkat cell line. *Int. Immunol.* **11**, 943-950.

Zhang, W., Sommers, C. L., Burshtyn, D. N., Stebbins, C. C., DeJarnette, J. B., Trible, R. P., Grinberg, A., Tsay, H. C., Jacobs, H. M., Kessler, C. M. et al. (1999b). Essential role of LAT in T cell development. *Immunity* **10**, 323-332.